COMPARATIVE STUDY OF DIASTOLIC FILLING UNDER VARYING LEFT VENTRICULAR WALL STIFFNESS

By

PRITAM SAI MEKALA

Bachelor of Science in Aeronautical Engineering

Vignan Institute of Technology and Aeronautical Engineering

Hyderabad, India

2013

Submitted to the Faculty of the
Graduate College of the
Oklahoma State University
in partial fulfillment of
the requirements for
the Degree of
MASTER OF SCIENCE
July, 2015

COMPARATIVE STUDY OF DIASTOLIC FILLING UNDER VARYING LEFT VENTRICULAR WALL STIFFNESS

Thesis Approved:

Dr. Arvind Santhanakrishnan

Thesis Adviser

Dr. Brian Elbing

Dr. Khaled A. Sallam

ACKNOWLEDGEMENTS

I take this opportunity to express my sincere and deepest appreciation to my committee chair, adviser, mentor and more importantly a great friend Dr. Arvind Santhanakrishnan. I thank him for introducing me to the wonders and frustrations of research. I thank him for his guidance, encouragement and support right from the beginning of this work. I thank him for his supervision and constant help, without which this thesis would not have been possible.

I would like to thank my committee members Dr. Brian Elbing and Dr. Khaled Sallam. They have provided, with kindness, their insight, suggestions and support, which are precious to me.

I place on record, my sincere thank you to Dr. Daniel Fisher, Department head, for the continuous encouragement.

I am also grateful to Aaron Alexander, Professor, in the Department of MET. I am extremely thankful and indebted to him for sharing his expertise, and valuable guidance all through my master's education.

Special thanks are due to all the past and present members of Applied Fluid Mechanics Laboratory (AFML) at Oklahoma state university. Especially, Audrey Pope, Damir Kolasinac, Matthew Takyi-Micah, Hong Kuan Lai, Joe Schovanec, and Milad Samaee for their support and friendship.

I also appreciate my school, Oklahoma State University, collaborators, Dr. Edward Martin and Dr. John Oshinski, and financial support from Oklahoma Center for the Advancement of Science and Technology (OCAST HR14-022).

Last but not the least, I thank my family, for encouraging me in all of my pursuits and inspiring me to follow my dreams. I am especially grateful to Annapurna Arunachalam and Arun Subbiah who supported me emotionally and financially. I always knew that you believed in me and wanted the best for me.

Name: PRITAM SAI MEKALA

Date of Degree: JULY, 2015

Title of Study: COMPARATIVE STUDY OF DIASTOLIC FILLING UNDER VARYING LEFT VENTRICULAR WALL STIFFNESS

Major Field: MECHANICAL AND AEROSPACE ENGINEERING

Abstract: Heart failure with preserved ejection fraction (HFpEF) is a clinical syndrome that is prevalent in over 50% of heart failure patients. Myocardial stiffening occurs in HFpEF patients prior to chronic maladaptive changes in overall chamber morphology, resulting in increased left ventricle (LV) wall stiffness. The goal of this study was to investigate the changes in intraventricular filling fluid dynamics inside a physical model of the LV as a function of wall stiffness and the presence of A-wave. The entire experiment was divided into 2 cases, inclusion of the A-wave and absence of A-wave during which three LV physical models of varying wall stiffness were compared. Physical model was incorporated into an in vitro flow circuit driven by a programmable piston pump. Windkessel elements were used to adjust the inflow and systemic pressure of the baseline LV model with lowest stiffness to match normal physiological conditions. The remaining two physical models with stiffer walls were comparatively tested without changing the in vitro circuit compliance, resistance and pump amplitude. 2D phase-locked particle image velocimetry (PIV) measurements along the central plane of the LV showed reductions in kinetic energy of the flow field, filling vortex ring circulation and inflow propagation toward the LV apex with increasing stiffness. For idealized mitral inflow profile without A-wave, hemodynamic characteristics including the peak filling velocity magnitude, cardiac output, stroke volume, and diastolic duration decreased with increasing wall stiffness. The same trends in hemodynamics were also observed with inclusion of A-wave to the mitral inflow profile. Further, inclusion of A-wave to the mitral inflow showed an increase in E/A (mitral inflow velocity peaks) ratio from 1.2 for the baseline (least stiff) LV model to 2.2 for the stiffest model, suggesting restrictive filling occurred in the latter. The results of the study show the adverse hemodynamic impact of pathological alterations in wall stiffness even when gross LV morphology is unchanged. The circulation strength of the intraventricular filling vortex can be potentially used as a fluid dynamic marker for improving diagnosis of HFpEF.

TABLE OF CONTENTS

Chapter Page

LIST OF TABLES

Table Page

Table Page

LIST OF FIGURES

Figure Page

Figure Page

Figure Page

Figure Page

Figure Page

NOMENCLATURE

AV	Atrioventricular
BMF	Blood mimicking fluid
BMHV	Bi-leaflet mechanical heart valve
BPM	Beats per Minute
CCW	Counter clockwise circulation
CFD	Computational fluid dynamics
CO	Cardiac output (L/min)
DCM	Dilated Cardiomyopathy
EDP	End-diastolic pressure (mm of Hg)
EOA	Effective orifice area
ESPVR	End-diastolic pressure-volume relationship
EDV	End-diastolic volume (mL)
EF	Ejection fraction
ESP	End-systolic pressure (mm of Hg)
ESPVR	End-systolic pressure-volume relationship
ESV	End-systolic volume (mL)
FOV	Field of view
GOA	Geometric orifice area
HCM	Hypertrophic cardiomyopathy

HF	Heart failure
HFpEF	Heart failure with preserved ejection fraction
HFrEF	Heart failure with reduced ejection fraction
HR	Heart rate
IVC	Isovolumetric contraction
IVR	Isovolumetric relaxation
LA	Left atrium
LAP	Left atrial pressure (mm of Hg)
LVEDV	Left ventricular end-diastolic volume (mL)
LV	Left ventricle
LVP	Left ventricular pressure (mm of Hg)
LVV	Left ventricular volume (mL)
MRI	Magnetic resonance imaging
PIV	Particle Image Velocimetry
PV	Pressure-volume
RA	Right atrium
RV	Right ventricle
SA	Sino-atrial
SD	Standard deviation
SV	Stroke volume (mL)
SW	Stroke work

CHAPTER I

INTRODUCTION

1.1 Clinical significance of the work

Despite advances in medical technology, heart failure is still a primary cause of death in the entire world [1, 2]. In America alone, heart disease has killed over 610,000 people in the year 2013 [3]. Out of all the registered cases, 30% - 50% are predominantly caused due to diastolic dysfunction, which has adverse effects on LV filling properties [4]. Impaired ventricular relaxation, decreased ventricular compliance, and increased atrial and ventricular filling pressures are some of the causes of diastolic dysfunction which can lead to reduced cardiac output (CO). Standard clinical metric called as ejection fraction (EF) is used to define cardiac health. EF is defined as the fraction blood ejected by ventricle with respect to end-diastolic volume (EDV). In this type of dysfunction, heart failure can occur with preserved ejection fraction (HFpEF), which makes it difficult to diagnose the disease. Despite the technological advances in intraventricular flow visualization techniques like noninvasive imaging [5-7], numerical [8] and experimental models [9, 10], several aspects pertaining to the relationship between LV compliance and hemodynamics [11-15] are still unclear. Hence there is a need for better understanding of the symptoms leading to heart failure and for methods of noninvasive assessment of the disease in an early stage.

1.2 Intraventricular vortex formation

Intraventricular filling fluid dynamics observed inside the LV of the human heart, varies with changes in LV wall stiffness. These changes have been proposed to indicate maladaptive function, even before structural changes are noticeable [16]. One of the important flow pattern inside the LV is a vortex ring, which is basically a circular region of fluid rotating perpendicular to the flow path. In normal conditions, blood flows into the LV throughout diastole via the mitral valve, forming a vortex ring. During systole, the primary vortex ring close to the intraventricular septum increases in size, elongating along the longitudinal axis; while the secondary vortex ring close to the anterior wall of the LV dissipates.

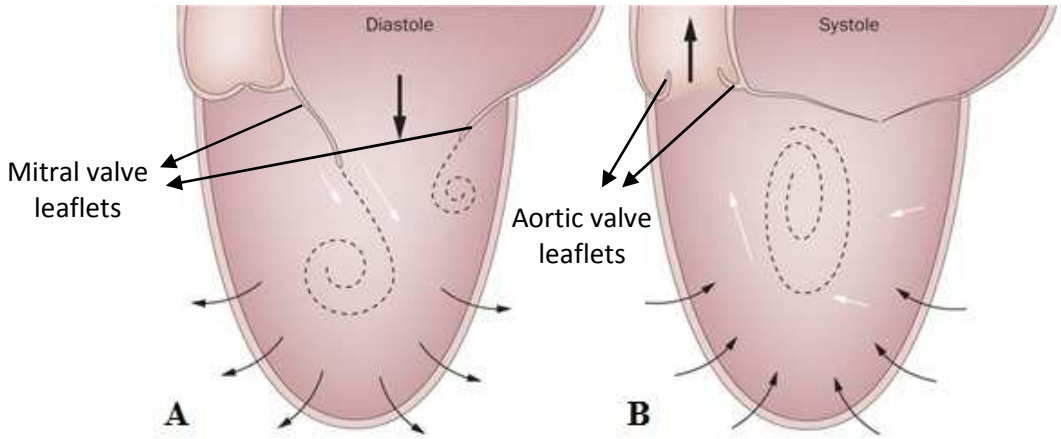

Figure 1: Direction of blood flow and fluid development inside LV. A) Shows a vortex ring inside the LV during diastole. B) Shows primary vortex ring inside the LV during systole (Pedrizzetti et al., 2014).

The primary vortex ring ensures smooth transition of the mitral flow towards the outflow tract whilst maintaining kinetic energy and longitudinal pressure gradients [16]. In diseased conditions, normal flow is impaired, altering the intraventricular fluid structures. These alterations result in inconsistent vortex ring formation and irregular flow patterns. An impaired flow pattern causes unnatural myocardial stress, which can trigger morphological maladaptation of the LV. An increase in myocardial stiffness prior to chronic maladaptive changes is the first step towards LV adaptation, resulting in increased wall stiffness.

1.3 Vortex Dynamics in LV under disease conditions

LV dilation, is a geometric adaptation in which the LV stretches and dilates, and is seen in diseases such as DCM. LV dilation reduces the ability of the heart to pump blood efficiently. Although the LV size is significantly larger, ejection fraction (EF) and stroke volume (SV) decrease drastically in the patients with DCM. In DCM, the vortex ring formed inside the LV is smaller in size and is mainly restricted to the center of the cavity.

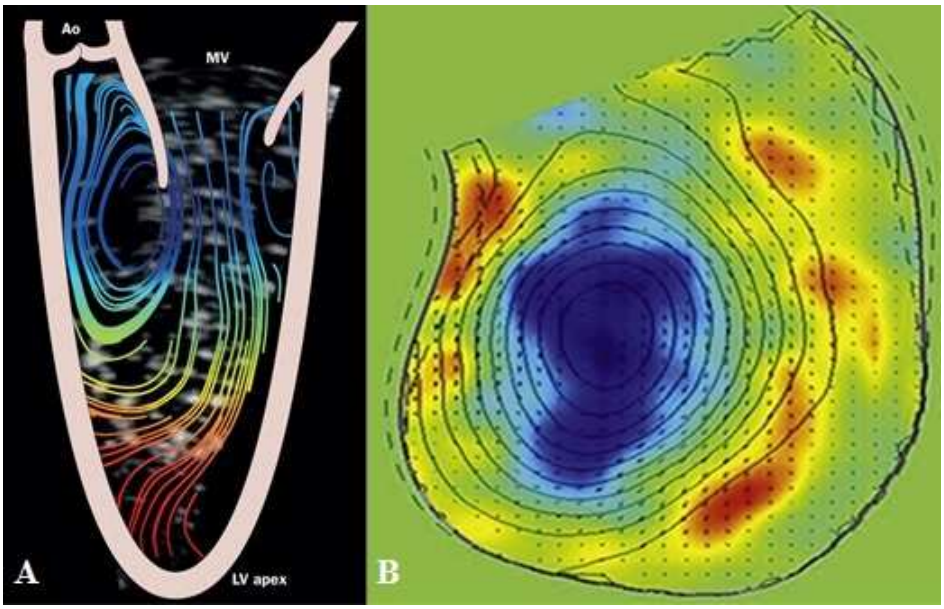

Figure 2: Vortex ring development inside LV. A) Shows elongated vortex rings inside the LV during diastole under normal conditions (Pedrizzetti et al., 2014). B) Shows primary vortex ring inside the LV during diastole in DCM (Kheradvar et al., 2010).

In DCM patients, the vortex wake formed during diastole maintains its compactness solely in the center of the cavity, inducing only local circulation [17, 18]. There are numerous previous studies available to help us understand the intraventricular fluid dynamics inside the LV during both normal conditions and disease conditions, where LV shape is altered (e.g. DCM) [19-23]. However, what exactly happens to intraventricular filling fluid dynamics during myocardial stiffness alteration with preserved LV shape is unknown.

1.4 Specific Aims

The purpose of this study was to investigate changes in intraventricular fluid dynamics during the filling phase of the cardiac cycle (diastole) as a function of changing LV wall stiffness, and A-wave. We hypothesized that, increasing LV wall stiffness will decrease CO and filling efficiency due to diminished inflow vortex strength. A series of four experiments were conducted to examine hemodynamics inside the LV using an in vitro phantom model and 2D Particle Image Velocimetry (PIV). During the experiment, the LV model with the least wall stiffness was tuned until it matched physiological conditions adapted from clinical measurements, and the results were then used as a reference for further investigations. Specific aims for these individual experiments are detailed below.

1. Investigate the changes in aortic pressure, inflow and outflow rates, CO, stroke volume, and vortex strength inside the LV as a function of left ventricular wall stiffness with the absence of A-wave at 70 BPM.
2. Investigate the changes in aortic pressure, inflow and outflow rates, CO, stroke volume, and vortex strength inside the LV as a function of left ventricular wall stiffness with the presence of A-wave at 70 BPM.

Comparison of hemodynamics inside the LV with and without A-wave as a function of varying LV wall stiffness.

CHAPTER II

LITERATURE REVIEW

Knowledge of normal cardiac structure is necessary in order to understand the complex diseases related to the heart. The following section is a review of cardiac and electric physiology.

2.1 Cardiac Structure

The heart is responsible for pumping blood inside the human body, whose importance was discovered by William Harvey, a medical doctor, fellow of college of physicians, and Lumleian lecturer. He observed the notion of heart in the living animals, which was published in his famous book "Exercitatio Anatomica de Motu Cordis et Sanguinis in Animalibus", commonly referred to as "de Motu Cordis" in the year 1628. The heart is a hollow muscular organ usually conical in shape, and it is situated in between the lungs and the pericardial layer. The average dimensions of a healthy human heart can measure up to 12cm in length, 8-9cm in diameter at the broadest region, and 6cm in thickness [24]. The total weight can range anywhere from 280 to 340 grams in males and 230 to 280 grams in females [25]. The geometrical and spatial structure of the heart are described below.

2.1.1 Human Heart

The human heart consists of a strong fibrous outer layer and an inner serosal layer filled with pericardial fluid, allowing it to function in a minimal-frictional environment [26]. This pericardial fluid compensates for changes in pressures and volumes, due to the presence of a constant volume outside the heart. In general, a human heart is divided into four chambers [27]: the Right Ventricle (RV) and Right Atrium (RA) on the right side, which are responsible for pumping deoxygenated blood from the entire body to the lungs, and the Left Ventricle (LV) and Left Atrium (LA) on the left side, which are responsible for pumping oxygenated blood from the lungs to the entire body. The ventricles are muscular chambers responsible for pumping blood into the lungs or throughout the entire body, whereas less muscular atria deliver blood to their respective ventricles. The right and left side of the heart communicate with each other through volume-pressure changes, although they are separated by an intraventricular and atrial septum.

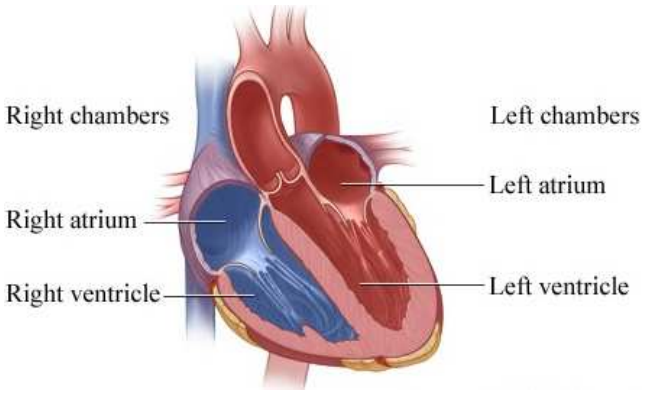

Figure 3: Picture shows the heart divided into two sides (left and right) and two chambers (ventricle and atrium) (University of Michigan Health System, Ann Arbor, MI, USA)

Oxygen deficit blood enters RA from the vena cava (superior and inferior) and flows into the RV through the tricuspid valve. RV then pumps the blood into the pulmonary artery through the pulmonary valve. The blood gets oxygenated in the lungs, which are located at the other end of the pulmonary artery. Oxygen rich blood is then pumped into the LA through pulmonary veins and into the LV through the mitral valve, which pumps it back into the systemic circulation through the aorta [28]. Four major unidirectional valves located inside the heart direct blood flow

in the forward direction, minimizing any chances of regurgitation. These valves are connected to the cardiac skeleton, a fibrous muscle structure composed of dense connective tissue.

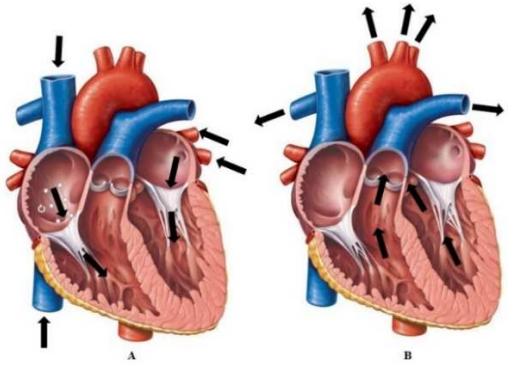

Figure 4: A) Arrows show the direction of incoming blood during diastole. B) Arrows show outgoing blood during systole. (Mayo Foundation for Medical Education & Research)

2.1.2 Internal Structure

The human heart is comprised of three different layers: the pericardium, myocardium and endocardium, from outside to inside [24, 29]. Each layer has different structures and functions that primarily aid in pumping action. The thickness of the heart varies in different regions; the ventricles are thicker compared to the atria, and the left side of the heart is thicker compared to the right side. These layers are discussed in detail below.

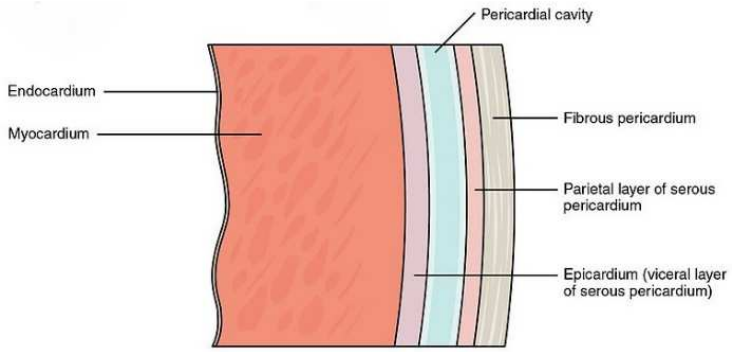

Figure 5: Picture shows different layers of the heart wall (Betts, J.G., et al, 2013)

2.1.2.1 Pericardium

The heart is enclosed inside a cavity called the pericardial cavity [24], which consists of two layers: the inner layer is called the visceral layer/epicardium and adheres to the outer layer of the heart. This visceral layer folds onto itself, forming a cavity called the parietal pericardium.

The empty region formed between the two pericardial layers is filled with a thin film of pericardial fluid, which allows the heart to function in a minimal-frictional environment. The pericardium is attached to the outer layer of the lungs, the pleurae, which help keep the pericardium and heart firmly anchored inside the thoracic chamber [29].

2.1.2.2 Myocardium

The myocardium is the thickest layer of the heart, consisting of bundles of cardiac muscle cells called cardiomyocytes. Muscle structures in the myocardium are similar to that of a skeletal muscle: surrounded by a sarcolemma, a plasma membrane in muscle, extending inwards, perpendicular to the length of the fiber. These sarcolemma form transverse tubes called T-tubules, which are studded with calcium channels. The level of calcium ions inside the calcium channels dictate different phases of the heart.

Myocardial cells, also called contractile cells, are made up of numerous myofibrils, measuring up to 25μm in diameter and 100μm in length. These are made up of long chains of individual sarcomeres, which are responsible for contractility of the heart walls. One of the important factors which determine the extent of myocardial shorting is the contractility of the cardiac muscle [30]. Each sarcomere is made up of two overlapping contractile proteins, called myosin and actin. Biochemical reactions take place inside these proteins, resulting in muscle contractions. During each cardiac cycle, these sarcomeres stretch from 1.5μm during ventricular systole to 2.2μm during ventricular diastole.

2.1.2.3 Endocardium

The endocardium is a thin serous membrane, which layers the inner region the heart. The cells inside the endocardium are similar to the endothelial cells that line blood vessels. They provide a smooth surface for the incoming and outgoing blood. Endocardium is known to act as a wall in between the blood and the heart wall, and also maintaining the pericardial fluid composition. Recent studies have shown that the endocardium can have control over the myocardial function of the heart.

2.2 Cardiac Function

2.2.1 Cardiac Cycle

The cardiac cycle consists of series of mechanical and electrical events that occur inside the heart, starting from one heartbeat to the beginning of the next heartbeat. The frequency with which the cardiac cycle occurs is called the heart rate (BPM). The cardiac cycle can be divided into five detailed stages which are described below.

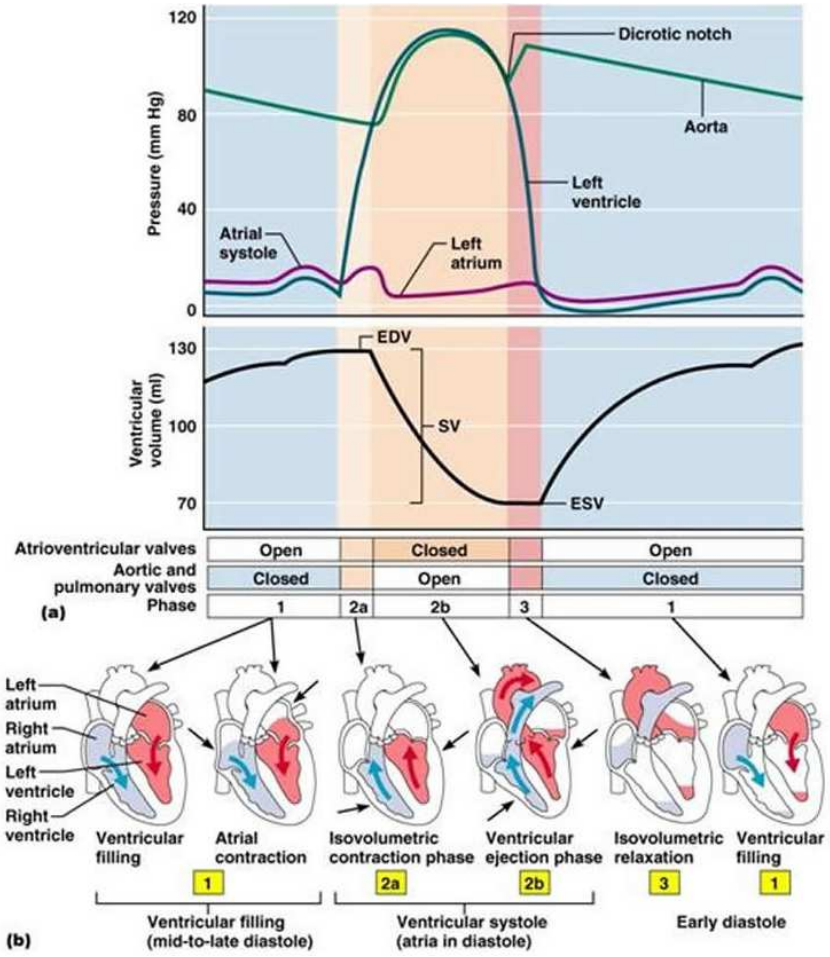

Figure 6: A) Temporal relationships between pressure and volume inside the chambers of the human heart. B) Corresponding atrial and ventricular activity inside the human heart during a normal cardiac cycle (Midlands Technical College, Columbia, SC, USA)

2.2.1.1 Diastole

During diastole (ventricular filling), the ventricles start relaxing, while oxygenated blood starts flowing passively from the lungs to the left atrium (LA) and deoxygenated blood enters the

right atrium from the superior and inferior vena cava. Blood then flows from the RA and LA into the RV and LV through the atrioventricular valves (mitral and tricuspid) that separate the atriums and ventricles.

The intraventricular pressure drops below the respective atrial pressure during the initial diastolic phase. Even though the ventricle gets filled with blood, the internal pressure does not fall because the walls are still undergoing relaxation. After the ventricular relaxation, the pressure slowly starts to rise, due to the inflow of blood being pumped from the atria through the atrioventricular valves. As the diastole approaches the end of the cycle, the atrial systole (A-wave) starts taking place, starting the cardiac cycle all over again.

2.2.1.2 Atrial contraction

During atrial contraction, the pressure inside the atrial chambers increases, forcing additional blood into the ventricles through the atrioventricular valves (mitral and tricuspid) that separate the ventricles and the atria. This atrial contraction causes a small pressure spike in the veins, known as an "a-wave" of the left ventricular atrial pressure.

Atrial contraction (atrial kick) is responsible for 10% of the left ventricular filling during diastole at resting conditions, while the remaining 90% usually takes place as the blood flows passively from the pulmonary veins and vena cava into the atria, then into the ventricles through the open atrioventricular valves. During increased heart rates, however, the atrial contraction accounts for almost 40% of the left ventricular filling. After the completion of atrial contraction, the atrial pressure decreases, causing the atrioventricular valves to return to their initial (closed) position. At this instant, the left ventricle has the highest volume of the entire cardiac cycle, known as the end diastolic volume (EDV). The left ventricular end diastolic volume (LVEDV) during resting condition is around 120 ml.

2.2.1.3 Isovolumetric Contraction

Isovolumetric contraction (IVC) starts after the closure of the atrioventricular valves. During this stage, myocardial cells start contracting, thereby resulting in an increase of pressure

inside the LV, without any change in the LV volume. LV volume remains constant, hence the term “isovolumic”, because all the valves are in closed position during this particular phase. The rate of increase in ventricular pressure is determined by the rate of contraction of the muscle fibers, which are determined by the degree of ion exchange in the calcium channels. Duration of an average isovolumetric phase in a healthy adult during resting condition is around 0.03 seconds [31]. Even though this duration is very minimal compared to the cardiac cycle, this short period of time is enough to generate pressures higher than those measured in the aorta and pulmonary artery, which helps maintain the unidirectional flow inside the ventricle.

2.2.1.4 Systole

Cardiac muscle cells of the ventricle contract rapidly during systole: the ejection or pumping phase of the heart. The ejection phase begins when the ventricular pressure exceeds the aortic and pulmonary pressures, causing the aortic and pulmonic valves to open. The blood is then ejected into the aorta, due to excess an energy gradient inside the ventricle compared to the aorta. The pressure gradient across the valve is typically very low because of the moderately large valve opening. During this phase, peak outflow velocities, as well as peak aortic and pulmonic pressures, are attained. The atrial pressures initially decrease, thereby causing the atrial chamber to expand and increase in volume. Blood from the respective venous inflow tracts start filling the atria, causing the atrial pressure to increase rapidly, which continues until the end of isovolumetric relaxation (IVR).

2.2.1.5 Isovolumetric Relaxation

IVR starts after the closing of the aortic valves, which usually follows backflow of blood into the ventricle from the aortic and pulmonary tracts. Immediately after the closing of the valves, the pressures inside the aortic and pulmonary tracts rise slightly, followed by a slow decline in the overall pressures. During this stage, myocardial cells start relaxing, thereby resulting in a decrease in pressure inside the LV, without any change in the LV volume. The rate of decrease in ventricular pressure is determined by the amount of relaxation of the cardiac

muscle fibers, which is called lusitropy. The volume contained inside the ventricle is now termed as “end systolic volume” (ESV), which, in healthy resting adults, is around 50 ml. The difference between end diastolic and end systolic volume (EDV – ESV) is called stroke volume. The atrial pressure continues to rise because of systemic circulation and inflow of blood from the lungs.

2.3 Electrophysiology

The electrical events occurring inside the cardiac muscle cells during a cardiac cycle are called the electrophysiology of the heart [32]. Electrocardiography is the process of collecting this electrophysiological data by implanting catheters inside the patient’s heart. Contraction or relaxation of the cardiomyocytes located inside the myocardium requires depolarization or repolarization of the cardiac cell membranes. During depolarization, the sinus node, which consists of pacemaker cells located at the intersection of the right atrium and superior vena cava, undergoes chemical exchange, thereby generating electrical impulses [33, 34]. The Sino-atrial node, also known as the SA node, is located in the myocardium, close to the epicardium. The electrical impulse that originates from the SA node travels to the atrioventricular node, which is situated between the atrium and ventricle. The atrioventricular node, also known as the AV node, is a very dense tissue that conducts electric impulse to the ventricles. After a delay of 0.12s, the electric impulse is then dispersed into the bundle of His, specialized heart muscle cells that help in conducting electricity further into the ventricles. The electric impulse finally reaches the purkinje fibers, conducting fibers larger than cardiomyocytes that possess the ability to transmit cardiac potentials more quickly and efficiently than any other cardiac cell. These fibers are responsible for creating synchronized ventricular contractions and are, hence, necessary to maintain the consistent heart rhythm.

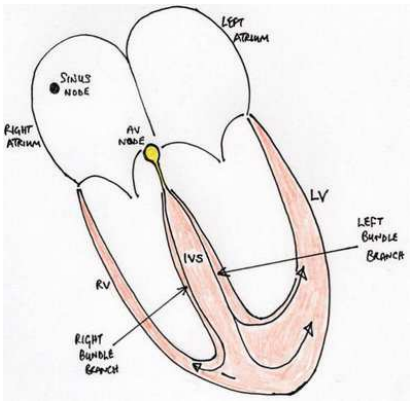

Figure 7: Basic electrophysiology inside a normal human heart (Dallas, 2010)

The series of electrical events described above can be illustrated using a typical electrocardiogram (ECG) tracing, a repetitive process of three major electrical impulses produced inside the heart. The first impulse is called a P wave and represents depolarization of the atria from the SA towards the AV node, which usually lasts less than 80ms. The next region in the graph is called a PR interval, which is defined as the amount of time it takes for the impulse to travel from SA to AV node. The PR interval usually lasts anywhere from 120 to 200ms. The electrical impulse, after reaching the ventricles, depolarizes rapidly, creating a QRS complex, which exhibit a larger amplitude, due to the fact that ventricles are thicker than atria. In healthy adults, the QRS complex lasts from 80 to 100ms. The J point is the instant when the QRS complex ends, and the ST segment begins. The next segment is called the ST segment, a depolarization segment connecting the QRS and the T-wave. The repolarization of ventricles is called a T-wave and lasts around 160ms during resting conditions. The interval between the beginning of the QRS complex and the apex of the T wave is called the absolute refractory period or vulnerable period [35]. The final region of the ECG curve represents repolarization of the interventricular septum, due to its lower amplitude it is completely absent in some individuals [35].

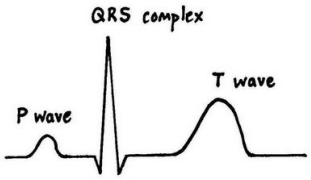

Figure 8: Basic schematic of major waves of a single normal ECG pattern (Dallas, 2010)

2.4 LV Fluid Dynamics

Intraventricular fluid dynamics are directly related to the CO of the heart; therefore, knowledge of these fluid characteristics is necessary to understand basic functions of the heart, especially the left ventricle. In today's world, analysis of intraventricular fluid dynamics is largely based on cardiovascular imaging techniques like magnetic resonance imaging (MRI), computed tomography and echocardiography. Although certain characteristics of these techniques can be appreciated, most are compromised. For example, MRI has the capability of producing high resolution images whilst lacking temporal resolution, whereas echocardiography makes up in temporal resolution with lacking images. Despite the technological developments in cardiovascular imaging tools, there is still a lack of detailed quantitative information about intraventricular fluid dynamics.

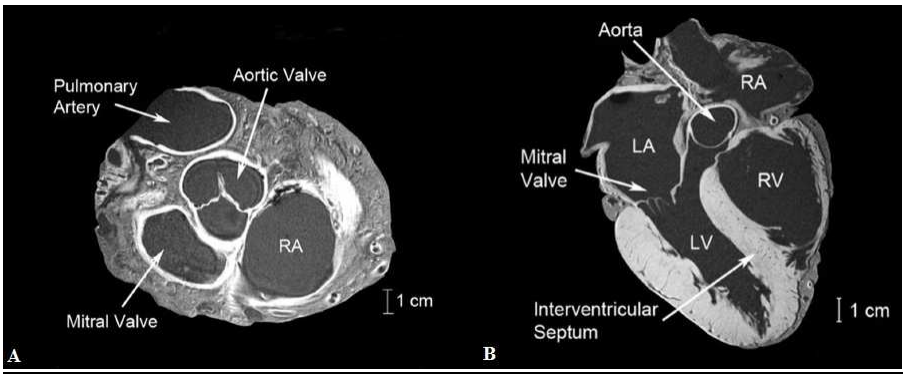

Figure 9: Image shows typical MRI scans: A) Short axis of the heart displaying all four chambers of the heart, the left and right atria and ventricles. B) Long axis view displaying all four chambers of the heart, the left and right atria and ventricles. (University of Michigan Health System, Ann Arbor, MI, USA)

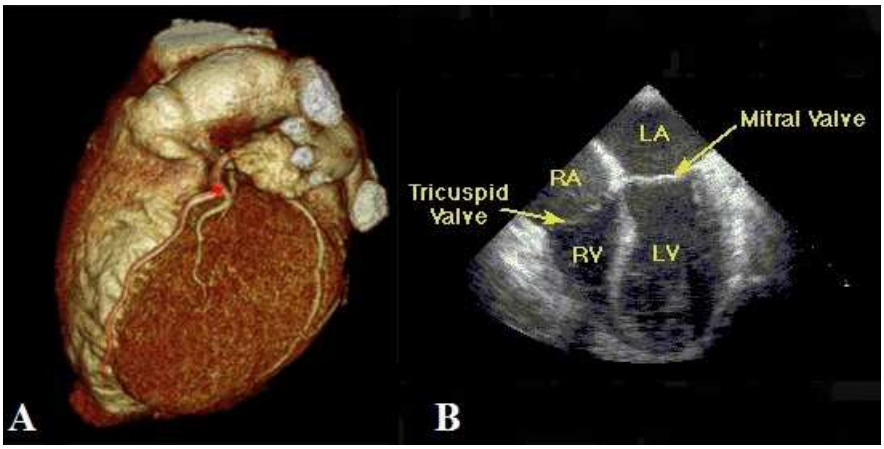

Figure 10: A) 3D view of a computed tomography scan of a normal human heart (Columbia University Medical Center, New York City, NY, USA). B) Typical echocardiograph scans showing all four chambers with atrioventricular valves (National Heart, Lung, and Blood Institute, Bethesda, MD, USA)

Numerical simulations can be used to predict approximate intraventricular flow characteristics by assuming simple models. These assumptions may use simplified models where changes caused to the surrounding tissues by fluid-tissue interactions and complex material properties, like non-linearity and time dependence, are ignored. Early numerical simulation models included axisymmetric approximations coupled with fluid-tissue dynamics with predefined tissue motion [36, 37].

Although assumptions like axi-symmetry might give preliminary results that help us understand the intraventricular fluid dynamics, they are usually not realistic interpretations because of the simplified LV geometry. A study on intraventricular fluid dynamics was performed on MRI data acquired on real human beings using computational fluid dynamics (CFD). Although MRI-CFD showed a feasibility among different flow quantification approaches, it lacked temporal resolution [38]. A recent study conducted on a three-dimensional flow structure inside an idealized artificial LV model during diastole showed formation of vortex rings near the inflow jet, followed by weak turbulence wake [8, 39]. A deeper investigation into the same model showed the relation between asymmetric flow and minimal energy dissipation inside the ventricle and, hence, maximum efficiency [40].

In general, LV flow consists of a strong inflow jet that enters the chamber through the mitral valve during filling phase (diastole) of the heart. This inflow jet is comprised of two stages: early ventricular filling (E-wave) and late systolic contraction (A-wave). The inlet jet comes in contact with the LV wall, and two vortex rings are produced on the either sides of the jet. During peak inflow, the inflow jet can measure up to 1 m/s, while extending several centimeters into the LV. These vortex rings have special asymmetric characteristics; the vortex ring close to the aortic valve increases in size and stretches longitudinally.

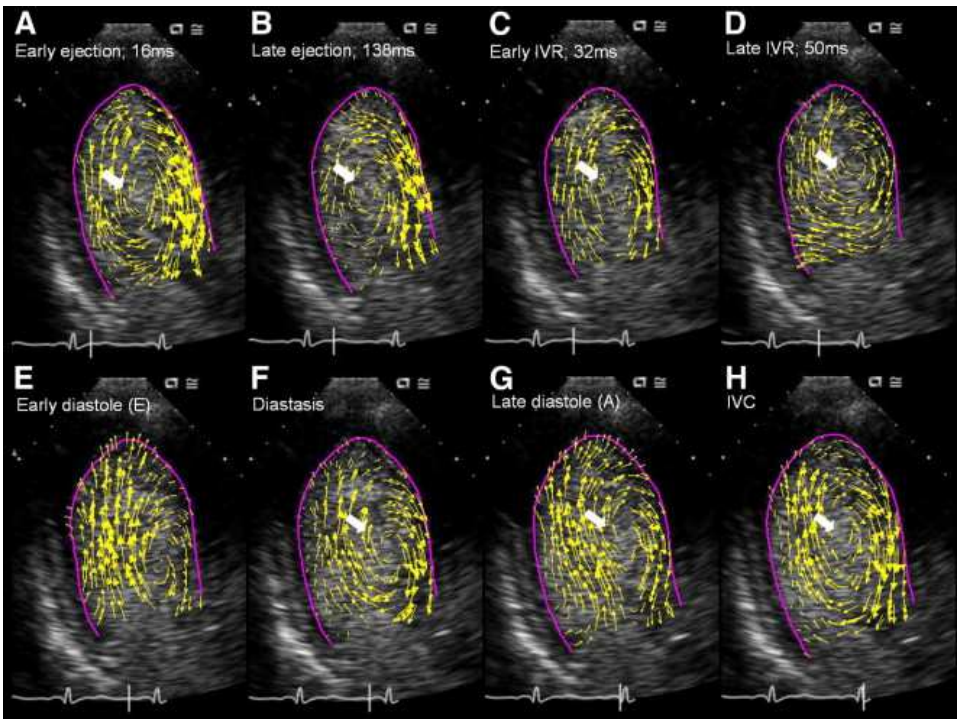

Figure 11: Numerical simulation of LV hemodynamics during a single cardiac cycle shows development of velocity vectors and LV vortex during diastole and systole (Geu-Ru., et al., 2008)

Studies show that the vortex ring close to the intraventricular septum is stronger and larger compared to the one close to the anterior wall of the LV. This asymmetric characteristic of the vortex ring not only helps in changing the direction of the inflow jet very quickly, but also aids in minimalizing the loss of the kinetic energy of the flow during systole. More recent studies show that this asymmetric vortex structure might allow a reciprocating, sling-like,

'morphodynamic' mode of action to come into effect when heart rate and output increase during exercise [41].

These intraventricular fluid properties can possess a variety of complex structures that have an impact on the overall cardiac function. For example, the length of the incoming jet can impact the endocardial tissues inside the LV, and pathophysiological conditions are impacted by the structure and position of the vortex ring inside the LV. In addition to the above mentioned effects, the geometry, elasticity and capacity of the heart can also play a fundamental role in intraventricular fluid dynamics. In the following chapters, we aim to investigate and understand the fluid dynamics as a function of varying LV wall compliance.

2.4.1 LV vortex

The LV vortex is a significant phenomenon that occurs regularly during a cardiac cycle. Clinicians, biologists, mathematicians, and fluid dynamists have been researching for decades to evaluate the intraventricular vortex, which is strongly related to CO and the geometry of the left ventricle [5, 7, 36, 42, 43].

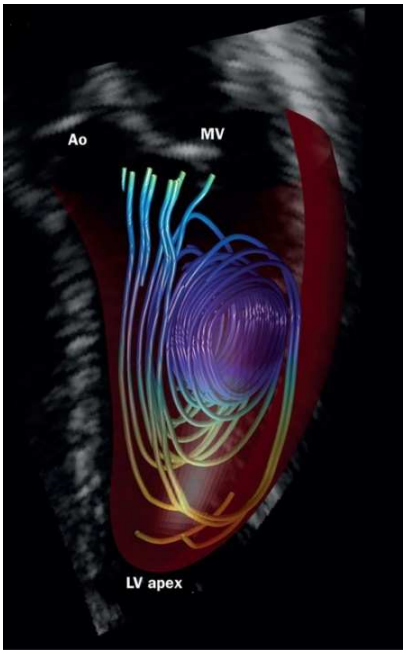

Figure 12: 3D streamlines reconstructed from multiplane acquisition at the onset of systole shows streamlines spiral out from the vortex and are directed towards the outflow tract. (Pedrizzetti, et al., 2014)

Vortex rings are complicated structures that create rapid accelerations, eccentricities and instabilities, whilst modulating energy and momentum transfer. The blood flows through the open mitral valve into the LV, where it becomes a high speed compact jet. The shear interactions between the high speed incoming jet and the stationary fluid inside LV cause the jet to roll clockwise into itself, forming a vortex ring-like structure [44]. Soon after the peak inflow jet is formed, the pressure gradient inside the LV progressively reverses until the pressure inside the apex exceeds the base. This process helps decelerate the incoming blood, while the vortex moves from the base to the center of the LV. The high pressure region created near the apex pushes the blood towards the outflow tract, while decreasing the incoming jet's velocity. This vortex ring has the capability to store part of the kinetic energy of the incoming fluid as rotational energy and guide it towards the outflow tract [45]. There has been a clear pattern in previous studies that shows the formation of the recirculating fluid region just underneath the atrioventricular valves. The recirculating region consists of a vortex pair, one more dominant than the other, giving rise to asymmetry inside the LV.

Natural asymmetry inside the LV is known to facilitate the overall CO and prevent stagnation (thrombus) inside the chamber. In healthy individuals, the major anterior vortex develops immediately after the beginning of early diastole and is preserved until late diastole [39]. It continues throughout IVC and dissipates with the opening of the aortic valve and LV ejection [46]. The vortex ring close to the anterior part of the LV is more dominant and, therefore, carries more significance in intraventricular fluid dynamics. Meanwhile, the weaker vortex ring, close to the posterior part of the LV, dissipates in the early phase of diastole. A recent study showed that the anterior vortex had a radius of 1.62 ± 0.24 cm (mean ± SD), an average angular velocity of 30.08 ± 9.98 radians/s, and maximal kinetic energy of 4.3 × 10^(-4) ± 7.1 × 10^(-5) J [7].

2.4.2 Altered LV vortex

Any changes in the geometry of the heart can alter the normal LV vortex structures and, hence, effect the overall CO. LV remodeling can exhibit a wide variety of adaptations, depending upon the type of disease: hypertrophic cardiomyopathy, dilated cardiomyopathy, etc. The changes that occur in the cardiac function due to LV vortex alterations are triggered by pathophysiological conditions or flow impairment and are discussed in detail below.

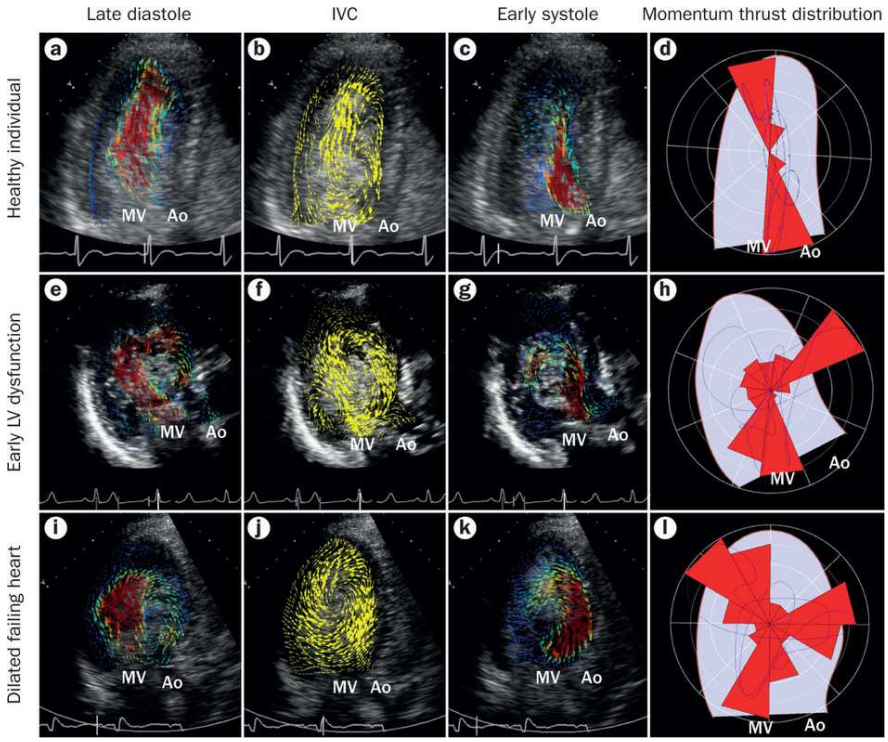

Figure 13: Figure shows changes in hemodynamic characteristics inside LV during different phases of the cardiac cycle compared between normal individual (a-d), patient with diastolic dysfunction (e-h), and patient with dilated cardiomyopathy (i-l). (Pedrizzetti, et al., 2014)

Diastolic dysfunction with preserved ejection fraction is defined as the inability of the LV to pump blood under normal circumstances when the ejection fraction ratio remains unchanged. Individuals with diastolic dysfunction underwent echocardiography, and their intraventricular flow was recorded digitally. This study showed that the vortexes formed inside the LV of these individuals were less coherent, more irregular and weakly turbulent, compared to healthy people. The incoming jet no longer comes in as a straight line, and the outflow adapts a curved path.

These fluid dynamic alterations cause the development of transversal forces and unnatural timings inside the LV [16].

LV remodeling means there is a change in the ventricular wall structure or LV obstruction caused by tissue overgrowth. It is primarily caused by abnormal loading conditions or genetic myocardial diseases. In the absence of self-compensating procedures, which the human heart generates in the event of a disease or an injury, LV remodeling becomes progressive and results in heart failure. The vortex ring adapts its shape and structure, depending upon the LV wall structure. Patients with dilated ventricle had similar changes in their flow, except the intraventricular vortex adapted a circular cross-section, thereby restricting the vortex ring close to the ventricle's base. This creates stagnation regions near the apex of the LV, causing apical thrombosis, which is usually associated with pathological blood streaming.

2.5 Left Ventricular PV loop

A Pressure-Volume (PV) loop is a graphical representation of the instantaneous relationship between pressure and volume inside the LV during a single cardiac cycle. Efficiency of the heart is directly related to the PV loop, so basic knowledge of the PV loop is necessary to diagnose any potential disease or malfunctions. The following paragraphs discuss the normal PV loop and altered PV loop behavior.

2.5.1 Normal PV loop

A cardiac cycle can be divided into four basic stages: diastole, isovolumetric contraction, systole, and isovolumetric relaxation. The PV loop shown below starts at point 1, when the ventricle is at maximum volume, thus representing the end-diastolic volume (EDV) and the end-diastolic pressure (EDP). The ventricle immediately begins isovolumetric contraction (stage 1), during which the mitral valve closes and LV pressure (LVP) starts rising, while the LV volume (LVV) remains constant (point 2). This gives rise to a vertical line until the opening of the aortic valve, which is followed by systole (stage 2). During stage 2, the LVP rises until it reaches peak value and then starts to decrease towards the end of the systole. LVV, on the other hand,

decreases constantly until the aortic valve closes (point 3). The ventricular volume at point 3 is at its lowest value, the end-systolic volume (ESV). During stage 3, the ventricle enters the isovolumetric relaxation (IVR) phase, in which the LVP decreases while the volume remains constant. At point 4, the mitral valve opens, and the ventricle starts filling (stage 4) due to the excess pressure gradient inside the LA.

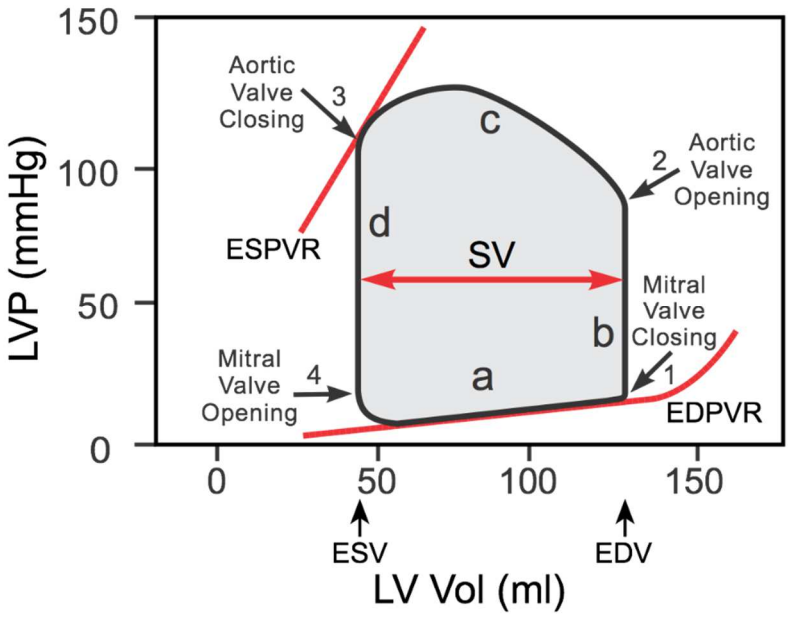

Figure 14: PV loop shows different phases of a cardiac cycle (Cardiovascular physiology concepts, Richard E. Klabunde, PhD)

The difference between the end-diastolic and end-systolic volume (width of the PV loop) is called the stroke volume (SV). SV can also be defined as the amount of blood being pumped by the heart in a single cardiac cycle. For a healthy individual, this value usually lies between 55-100 ml [47]. The area of the region occupied by the PV loop is called the ventricular stroke work. Cardiac output (CO) is the volume of blood being pumped by the heart in a minute and is obtained by multiplying SV and heart rate (HR). An average resting CO was found to be 5.6 L/min in males and 4.9 L/min in females [48]. Ejection fraction (EF), the efficiency of the heart, is defined as the ratio of SV to EDV. For a healthy individual, this value usually lies between 55-70% [47]. The mechanical load experienced by the ventricle during systole and diastole are defined as afterload and preload, respectively. Afterload is hugely dependent on ESV and ESP,

whereas preload is dependent on EDV and EDP. Stage 4 represents EDPVR (end-diastolic pressure-volume relationship), which follows along the filling path of the ventricle. The slope corresponding to EDPVR is equivalent to the stiffness of the heart wall [dP/dV]. Compliance is the term generally used in cardiovascular physiology to represent heart wall stiffness, which is the reciprocal of stiffness$[\mathrm{dP/dV}]^{-1}$. The maximum LVP that can be achieved in stage 2 is called ESPVR (end-systolic pressure-volume relationship), which represents the contractility of the heart. Therefore, in a healthy individual, the PV loop never crosses the EDPVR and ESPVR under a given inotropic condition.

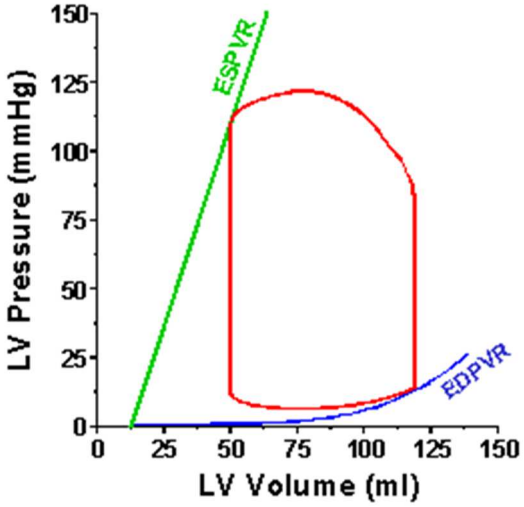

Figure 15: EDPVR and ESPVR providing a boundary in which the PV loop falls at the end of the cardiac cycle (Courtesy of Columbia University, NY, USA)

2.5.2 Altered PV loop

Knowledge of the PV loop is necessary in order to understand basic changes in ventricular functions. The PV loop is dependent on multiple parameters, like preload, afterload and contractility of the cardiac muscle cells. These parameters are mutually dependent on each other: changes in one parameter affect the others significantly.

2.5.2.1 Effects of preload

Preload is the maximum amount of stretch the ventricles (right/left) can achieve during the end of diastole. In other words, it is the maximum stretch the cardiomyocytes can attain at

end-diastolic volume. Since the ideal length of sarcomeres cannot be measured while the heart is working, parameters like EDV and EDP are used. In order to increase the preload while the afterload and contractility are maintained constant, the end-diastolic volume should be increased. The net effect will cause the heart to pump more blood in a single cycle, thereby increasing the SV, represented by a wider PV loop, resulting in increased ejection fraction. The unique ability of sarcomeres to return to the same length even though the muscle preload increases, causes the ventricle to contract to the same ESV. Similarly, decrease in the preload is achieved by lowering the EDV, which results in decreased SV, SW and EF.

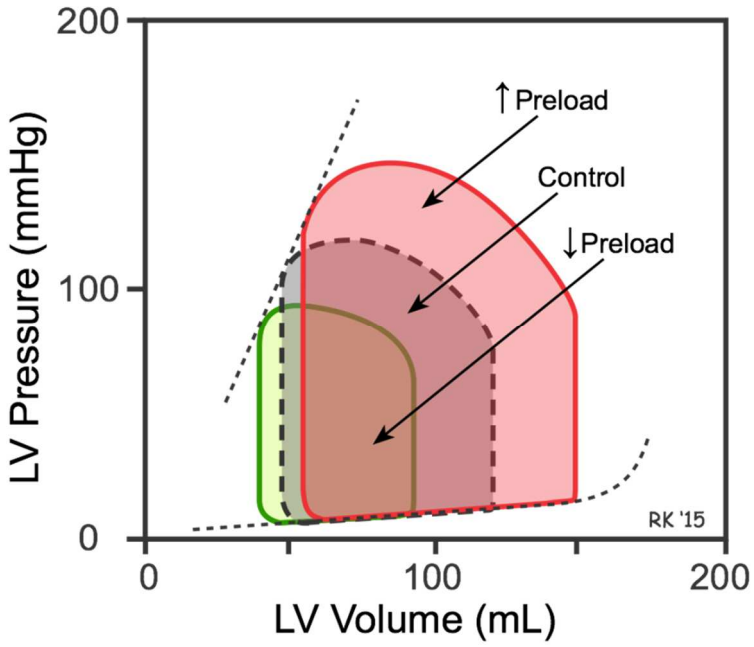

Figure 16: Figure illustrates changes in PV loop during the corresponding changes in preload (Cardiovascular physiology concepts, Richard E. Klabunde, PhD)

2.5.2.2 Effects of afterload

Preload is directly proportional to the aortic pressure in the LV and the pulmonary pressure in the RV: increase in aortic/pulmonary pressure results in increased ventricular pressure. In this case, the effects of afterload are verified, while the preload and contractility of the LV chamber are maintained constant. Increase in afterload reduces the velocity with which the cardiac muscle fibers contract, and, hence, the peak velocity of the outflow decreases. This usually results in a decrease in stroke volume (along the path of passive filling curve) and an

increase in ESV (along the slope of ESPVR). The reduced SV, increased ESV and increased LVP cause a significant drop in ejection fraction. On the contrary, a decrease in after load results in increased stroke volume and decreased ESV and LVP, which results in increased ejection fraction. These effects are illustrated in the pictures shown below.

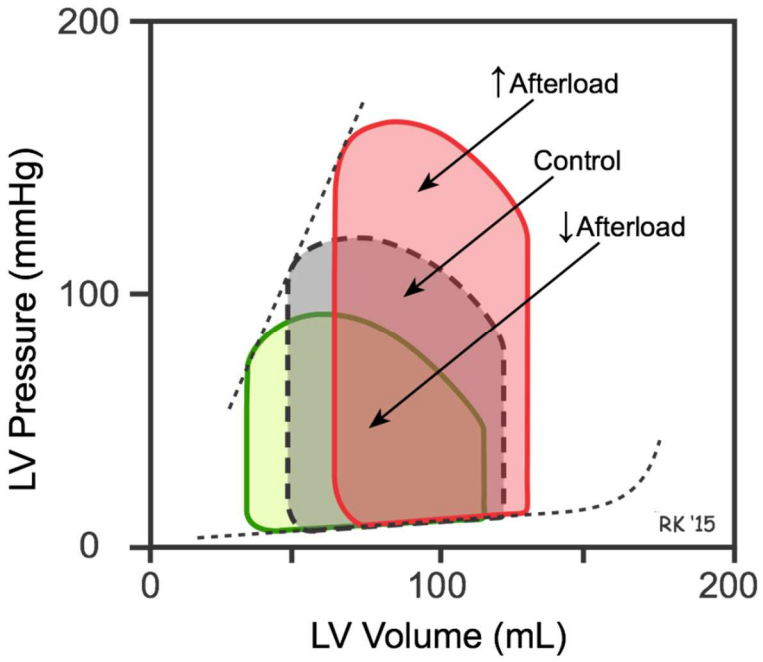

Figure 17: Figure illustrates changes in PV loop during the corresponding changes in afterload (Cardiovascular physiology concepts, Richard E. Klabunde, PhD)

2.5.2.3 Effects of contractility

Contractility, also known as inotropy, is defined as the force or energy with which the cardiac muscle contracts. Increase in contractility causes the ventricles to maintain the ESP whilst decreasing the ESV. This results in an increase in the rate of pressure inside the ventricle and the corresponding ejection velocity. The stroke volume and ejection fraction increase simultaneously with the increase in LVP. The PV loop diagram clearly shows the increase in the slope of ESPVR with the increase in contractility. A decrease in contractility has opposite effects, like increase in ESV and decrease in stroke volume and ejection fraction for a given preload and afterload.

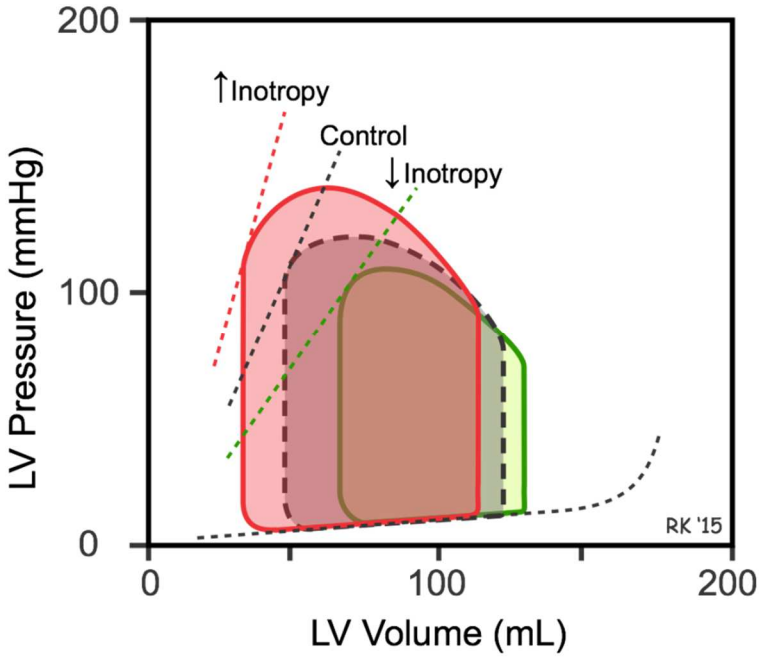

Figure 18: Figure illustrates changes in PV loop during the corresponding changes in inotropy (Cardiovascular physiology concepts, Richard E. Klabunde, PhD)

2.6 Cardiomyopathy

Cardiomyopathy is a group of diseases caused by the inability of the heart to pump blood to the lungs and body. Cardiomyopathy is associated with changes in geometry, muscle mass and elastic nature of the myocardium, which can lead to physiologic diastolic dysfunction. These are generally classified into two types: dilated cardiomyopathy and hypertrophic cardiomyopathy. There is a third kind, a combination of certain disorders, referred to as restrictive cardiomyopathy. This study focuses on hypertrophic cardiomyopathy wherein changes in left ventricular fluid dynamics are observed as a function of wall stiffness.

2.6.1 Dilated Cardiomyopathy

Dilated cardiomyopathy (DCM) is a common cause of congestive heart failure because of left ventricular dilation. In this particular condition, the heart wall becomes weaker and enlarged (end-diastolic volume >250 mL [49]), therefore losing the ability to pump blood efficiently. The cause of DCM is usually unknown, which makes it incredibly difficult to diagnose. Impaired

blood flow during systole usually triggers DCM, leading to progressive adaptation (enlargement). This results in increases in LV EDV and ESV, wall thinning, restricted wall motion and LV remodeling.

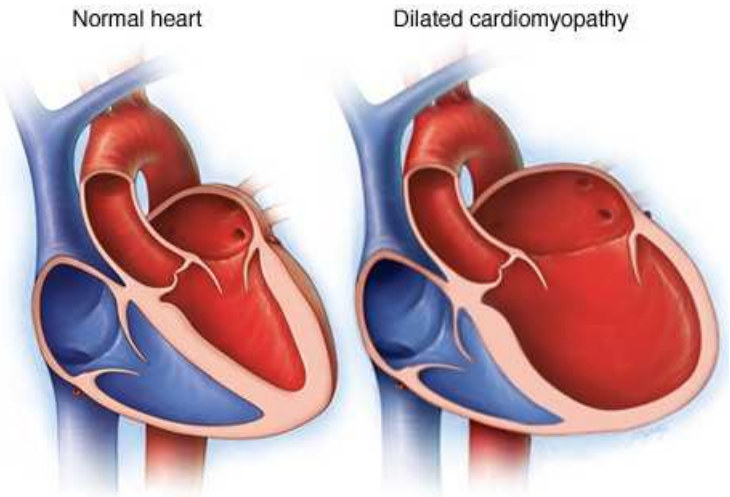

Figure 19: Picture shows the changes in LV geometry due to dilatation compared to a healthy individual (Mayo foundation for medical education and research)

The factors effecting LV filling are the atrioventricular pressure gradients during early diastole. Recent studies have shown a relation between the peak ventricular velocity and atrioventricular pressure gradients [50]. Pulsed wave Doppler recordings at mitral annulus revealed that with LV dilation, peak E and A-waves change, depending upon the left atrial pressure (LAP) gradient. When the LAP is normal, the early diastolic filling reduces, followed by a delayed mitral valve opening, an elongated IVR, and a lower dissipation of atrioventricular pressure [51-53]. Because of the reduction in early diastolic filling, the contribution of A-wave towards diastole increases. On the other hand, an increase in LAP causes an increase in peak E-wave velocity and a decrease in peak A-wave velocity simultaneously, thereby reducing the length of isovolumetric relaxation and the acceleration time for the peak inflow. These changes in intraventricular fluid dynamics cause an increase in E/A ratio, mitral regurgitation, and left atrial pressure, which, as a result, lower the CO and stroke volume among patients with DCM [54].

2.6.2 Hypertrophic Cardiomyopathy

Hypertrophic cardiomyopathy (HCM) is one of the major causes of diastolic dysfunction, wherein the heart muscle thickens without any recognizable reasons, and creating functional impairment in the cardiac muscle. HCM usually affects the left ventricular portion of the heart, and during this condition, the heart wall increases more than 30 mm [55]. This usually causes changes in normal cardiac filling patterns, which results in impaired LV relaxation, where the E/A ratio increases with decrease in compliance [56].

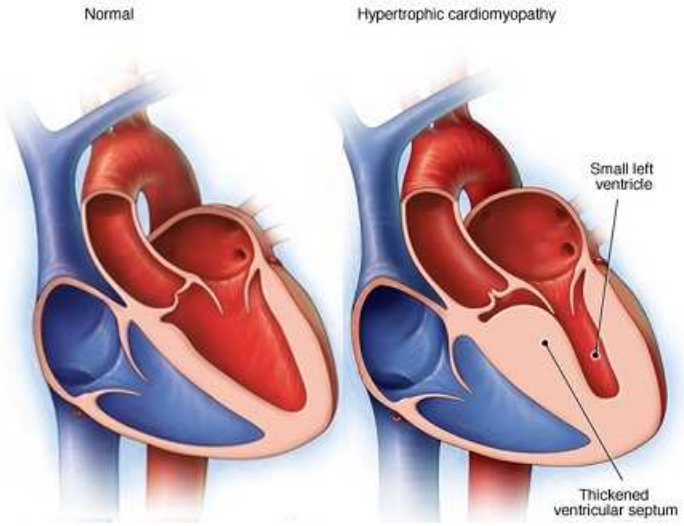

Figure 20: Picture shows the changes in LV geometry during hypertrophy compared to a healthy individual (Mayo foundation for medical education and research)

Patients diagnosed with HCM have a narrow outflow tract area (average 2.6-5.9 cm^2) compared to healthy individuals (average 10.4 cm^2) [57]. Due to the narrow outflow tract, early systolic flow experiences higher ejections, causing a local under pressure in the outflow tract, thereby elevating the mitral leaflet into the septum by means of venture mechanism [58, 59]. Local under pressure causes the ventricle to experience negative flow, which denotes the presence of coherent turbulent flow structures and vortices inside the chamber. These intense coherent turbulence structures induce dissipation, thus reducing the ability of the ventricle to recover from pressure losses. In conclusion, patients diagnosed with HCM will experience reduced outflow

velocity, due to the increase in local pressure and drag, resulting in reduced CO and stroke volume.

2.7 Heart Failure

Among all the patients diagnosed with heart failure, 50% of them have a preserved ejection fraction (HFpEF), whereas the rest display reduced ejection fraction (HFrEF) [60, 61]. The current study is based on measuring intraventricular fluid dynamics during diastolic dysfunction which is associated with heart failure with preserved ejection fraction.

2.7.1 Heart Failure with reduced EF

Ejection fraction plays an important role in healthy functioning of the heart and reduction in EF can lead to restricted CO which results in death in most cases. HFrEF is defined as the heart failure with EF $\leq$ 40%, whereas the normal range of EF in healthy individuals was measured to be around 55-70% [62]. In HFrEF, the LV dilates into an eccentric shape resulting in large LVEDV. Furthermore, in HFrEF, LV elastance reduces and atrial elastance increases causing impairment in ventricular-vascular coupling which reduces the efficiency of energy conversion from systole to stroke work [63, 64]. Recent study conducted on HF showed decrease in a dimensionless index vortex formation time (VFT), a fluid property representing efficiency of fluid propagation inside the LV [65].

2.7.2 Heart Failure with preserved EF

HFpEF is defined as heart failure with impaired diastolic function whilst in the presence of normal LV systolic function. LV diastolic dysfunction occurs due to increased myocardial stiffness which can transmit to other cardiac cells via matricellular proteins. Prolonged IVR, slow diastole, and increased LV wall stiffness are few basic symptoms of HFrEF [66-68]. LV wall with higher than normal stiffness is generally associated with reduced CO during atrial stress and exercise conditions [69-71].

During this condition, stiffness induces elevation in the afterload causing increase in ESP which worsens diastolic relaxation triggering prolonged adaptation. Combined ventricular and atrial

stiffening during HFpEF leads to changes in peak EDP by altering its slope and/or position of EDPVR.

CHAPTER III

EXPERIMENTAL SETUP

3.1 Physical model

The LV dimensions (long and short axis) used to design the physical model are shown in the **Table 1**. Values of anatomical dimensions corresponds to the data acquired from echocardiography conducted on real humans.

Axis	Real-dimensions (cm)	LV model dimensions (cm)
Long axis (LV basal-apical length)	10	9.2
Short axis (LV diameter)	4.2–5.9	4.83

Table 1: Anatomical LV (Lang, R.M., et al., 2006) (Frank, O., 1990) and LV physical model dimensions across long and short axes

The physical model was designed in SolidWorks (Dassault Systèmes SolidWorks Corp., Vélizy, France). The first phase of designing was to divide the model into several layers, from the base to the apex, and each layer was individually designed, using dimensions acquired from previous studies [72] (**Figure 21**a). Splines were used to constrain the model both length-wise and width-wise, giving the model its unique shape (**Figure 21**b). These layers were then joined together from the base to the apex, yielding a solid piece, as shown in the **Figure 21**c.

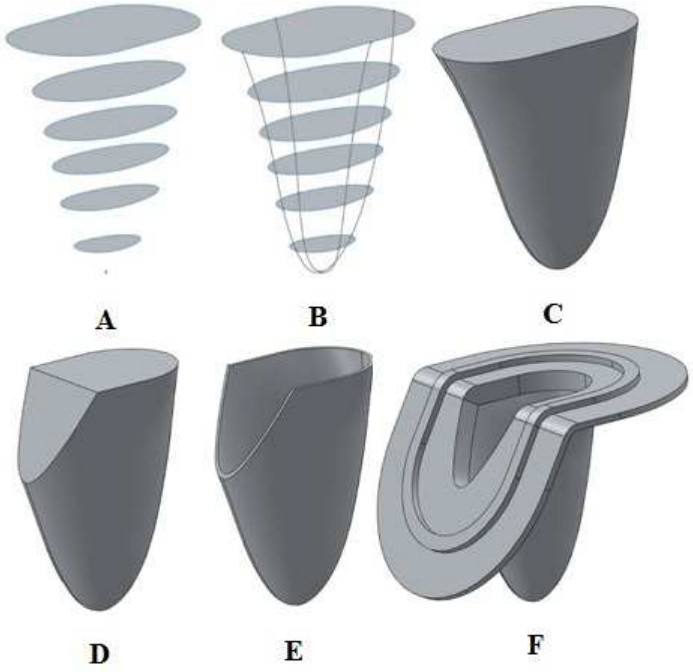

Figure 21: LV physical model design in SolidWorks (Dassault Systèmes SolidWorks Corp., Vélizy, France): A) LV physical model divided into horizontal layers. B) Splines used as constrains both lengthwise and widthwise. C) LV physical model as a complete solid structure. D) Angled cut exposing the aortic and mitral openings. E) Hollow model after "shell" command. F) LV physical model with flanges at the opening surfaces for attachment and sealing

An angled cut was then made across the short axis, extending through the entire width of the model, which later acts as an opening for the aortic valve (**Figure 21**d). A unique feature called "shell" later enabled the creation of a 1.5mm thick bag-like structure, as shown in the **Figure 21**e. Finally, "U" shaped flanges were designed on the either sides of the openings, which allows the physical model to be hoisted in any direction (**Figure 21**f).

3.2 Flow loop

In order to study the hemodynamic characteristics inside the human LV from an engineering perspective, a model representing an idealized cardiovascular system was considered. A two-element Windkessel model consisting of compliance and resistance, was chosen for the current experiment.

3.2.1 Windkessel

The term Windkessel in German means “air chamber” [73, 74], and this model was introduced by Otto Frank, a German physiologist in the year 1899. He described the heart and the systemic arterial system as a closed hydraulic circuit. In general, this model consists of a Windkessel chamber, filled with fluid and air which helps attenuate fluctuations in blood pressure over entire cardiac cycle resembling the elastic nature of blood vessels, a peripheral resistance which refers to the flow resistance encountered by the blood as it flows through the systemic arterial system, a reservoir and a pump.

Elasticity in blood vessel is represented by a term called compliance which is the reciprocal of stiffness. Whereas, the resistance is represented in terms of energy dissipating resistor. Mathematically, compliance is defined as the change in volume (ΔV) divided by the change in pressure (ΔP) (cm3/mmHg) and resistance is described as the change in pressure (ΔP) divided by change in volume (ΔV) per second (mmHg*s/cm3), see equations below.

$$C = \frac{\Delta V}{\Delta P} \quad \{1\}$$

$$R = \frac{\Delta P}{Q} \quad \{2\}$$

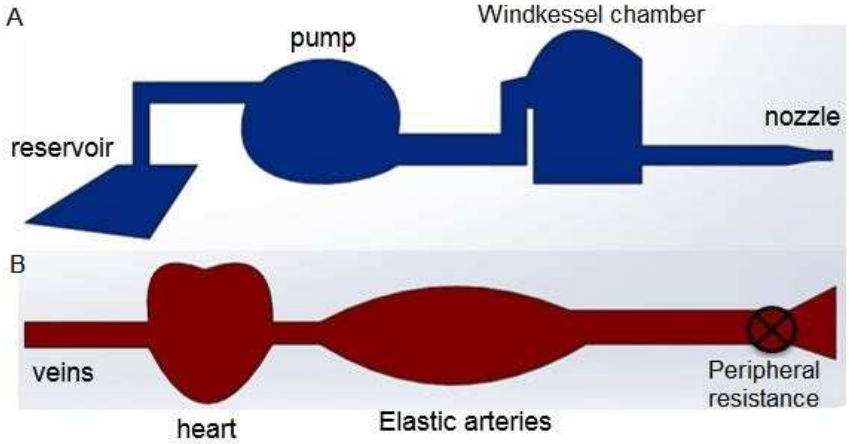

Figure 22: Windkessel model (A) represents the cardiovascular system (B) in its simplest form (Saouti, N., et al., 2010)

3.2.2 Flow loop setup

The experimental setup consisted of a pressurized LV chamber that contained the physical model inside (**Figure 23** B). The LV chamber was connected to a compliance chamber (**Figure 23**), which, in turn, was connected to the resistance and reservoir. Finally, the reservoir was connected back to the LV chamber, thereby creating a closed loop. This flow loop was driven externally by supplying $V(t)$ to a programmable piston pump (SuperPump ViVitro Labs Inc., Victoria, BC, Canada). The LV chamber was filled with blood mimicking fluid (65% glycerin – 35% water mixture). This fluid mixture was chosen to mimic the kinematic viscosity of blood, which ranges in between 2.8 – 3.8 x $10^{-6}\mathrm{m}^2/\mathrm{s}$ [75]. The fluid kinematic viscosity was 3.55 x $10^{-6}m^2/s$ and density was 1.16745 kg/m^3 during our study.

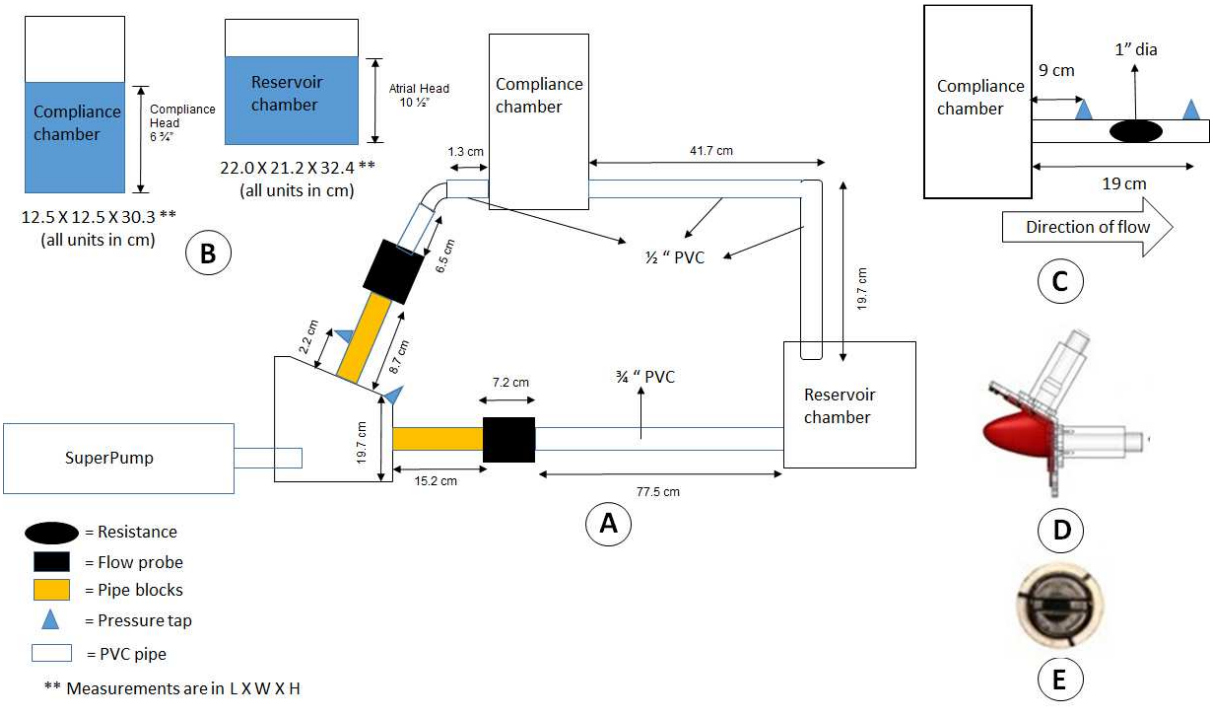

Figure 23: A) Detailed schematic of experimental setup B) Isolated compliance and reservoir chamber shows liquid levels and total chamber volume C) Isolated compliance chamber shows position of pressure taps and resistance D) LV physical model isolated from the flow loop shows the direction of inflow and outflow c) Bi-leaflet mechanical heart valve (BHMV)

Figure 24: Programmable piston pump (ViVitro Labs Inc., Victoria, BC, Canada) used to run the flow loop

3.2.3 Pipe connections

All the equipment pertaining to the flow loop are connected using flexible pipes and PVC pipes of varying lengths and diameter (

Table 2).

Pipe type	Pipe size [in]	Pipe purpose
Flexible Standard-Wall Clear Unthreaded Pipe	1	Joining the inlet and outlet pipe blocks to the flow loop
Flexible Standard-Wall Clear Unthreaded Pipe	1 ¼	Joining the SuperPump with the LV chamber
Schedule 40 PVC pipe	¾	Used on the either sides of the compliance chamber
Schedule 40 PVC pipe	1	Divides flexible pipe joining SuperPump and LV chamber
Schedule 40 elbows 90° Female Unthreaded	1	Joining the SuperPump with the LV chamber
Schedule 40 elbows 90° Female Unthreaded	1 ¼	Joining the compliance chamber to the reservoir
Schedule 40 pipe Tees - Female Unthreaded	1 ¼	Joining the drain valve to LV chamber
Schedule 40 PVC reducing coupling Female Unthreaded	1” – ¾	Joining the LV chamber to the reservoir

Table 2: Types and sizes of pipes used in the flow loop

3.3 Heart valves

Two BMHV's (Regent™, St. Jude Medical, Inc., St. Paul, MN, USA) were used in the experimental setup. These valves are composed of two flat, semi-circular occluders known as leaflets. Within the annular housing, each leaflet has an extension known as the "leaflet ear", which pivots about struts attached to the valve housing [76]. The pivot geometry consists of two arc-shaped notches at either end of each leaflet and spherical protrusions at four places on the orifice [77]. These arcs limit the opening and closing angles of the leaflets and also eliminate any support required by them. When the leaflets are open, blood flows through the central rectangular orifice and two lateral semi-circular orifices of the valve, making an 85 degree angle with the plane of the orifice ring [78-80]. When the leaflets are closed, small openings between the semi-circular discs, called B-datum gaps and peripheral gaps, allow some degree of leakage through them [76], leakage may also occur in and around the hinge regions. The angle between the leaflets is 120 - 130 degrees when they are closed, whereas the angle is only 10 degrees when they are open [81].

Figure 25: Bi-leaflet mechanical heart valve: Top view. (St. Jude Medical, Inc., St. Paul, MN, USA)

The leaflet housing and the leaflets are made of graphite coated with pyrolytic carbon [82]. The valve sewing cuff is constructed of double velour polyester fabric, which is mounted on the orifice using a titanium stiffening ring secured with two lock rings and a lock wire [83]. The central leaflet opening provides for a large effective orifice area (EOA) [78, 79], and the resulting

blood flow across the valve is a near laminar flow, which gives excellent hemodynamic conditions. The regurgitant flow washes the valve during the end of filling and pumping phases, thereby minimizing thrombosis. The valve design preserves the hemodynamic characteristics and also provides the least amount of resistance to the incoming flow. Lower pressure gradients across these valves, increased geometric orifice area (GOA), improved performance, making them very desirable [78, 79]. Exceptional durability, no structural failures up to 10 years from the point of inception inside a human heart, and MRI compatibility are other added advantages of these heart valves [84].

3.4 Pressure measurements

The following equipment were used to measure the pressure inside the LV chamber, LV physical model, and resistance elements used in the flow loop.

3.4.1 Pressure Transducer

Deltran® Disposable Pressure Transducer (**Figure 26**A) (Model number: DPT-200. Utah Medical Products Inc., Midvale, UT, USA) was used to measure the total pressure inside the ventricle and the aortic outflow. Deltran® Disposable Pressure Transducer consists of four important parts: pressure transducer, zeroing stop cock, flush device, and non-compliant pressure tubing. All the pressure transducers are primed and zeroed with respect to the atmospheric pressure before beginning the data acquisition process during every experiment. Delta-Cal™ Pressure transducer simulator/tester (**Figure 26**B) (Model number: 650-950. Utah medical products Inc., Midvale, UT, USA) was used to calibrate the above mentioned transducer.

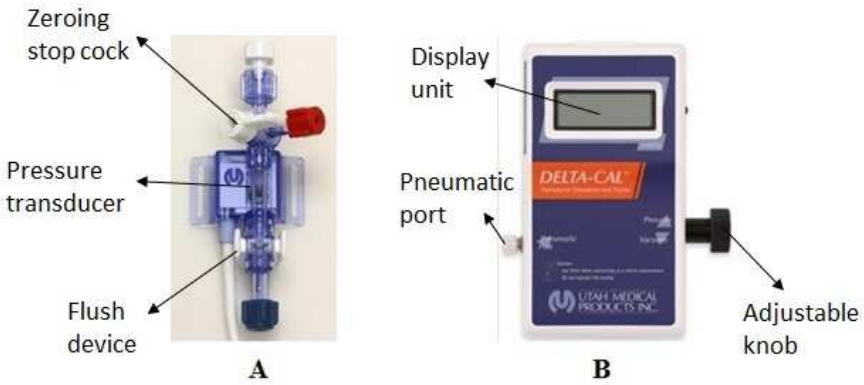

Figure 26: A) Deltran® Disposable Pressure Transducer. B) Delta-Cal™ Pressure transducer simulator/tester (Utah Medical Products, Inc., Midvale, UT, USA)

3.4.2 Signal Conditioning Module

Signal conditioning module used to amplify the voltage measured by the pressure transducer.

3.4.2.1 Signal conditioning module case

Signal Conditioning Module Case (figure 22A) (Model number: MC170-L. Validyne Engineering, Northridge, CA, USA) was used in the experimental setup to amplify, filter and output recorded pressures as digital values. Manufacturer specifications for this signal conditioning module are given below:

Specifications	
Output Signal	+/-10 VDC
Input Power Requirement	10 to 36 VDC, 8 slot: 20 W, 16 slot: 30 W
Carrier Oscillator	5 Vrms @ 3 KHz, 2 W

Table 3: Manufacturer specifications for MC170-L mobile module case (Validyne Engineering, Northridge, CA, USA)

A B

Figure 27: A) MC170-L mobile module case. B) Model SG297A Strain Gage Conditioner. (Validyne Engineering, Northridge, CA, USA)

3.4.2.2 Strain Gage Conditioner

Model SG297A Strain Gage Conditioner (figure 22b) (Validyne Engineering, Northridge, CA, USA) was used in the experimental setup. This strain gage signal conditioner consisted of a DC amplifier, bridge excitation circuit, bridge balance, shunt calibration network, low pass filter and output stage. Manufacturer specification for these signal conditioners are given below:

Specifications	
Input	1mV/V -50mV/V, switch selected
Sensitivity	in 1, 2.5, 5 - sequence
Gain Vernier	0.3 to 1.3 X range
Bridge Excitation	5 or 10V excitation.
Differential Input Impedance	Greater than 10 mega Ohms
Bridge Balance	+/-2mV/V with 350 Ohm bridge
Output	+/-10Vdc, 0 to +/-2mA
Output Resistance	< 10 Ohms

Table 4: Manufacturer specifications for Model SG297A Strain Gage Conditioner (Validyne Engineering, Northridge, CA, USA)

3.5 Flow measurements

The flow rates inside the flow loop were measured using ultrasonic flow measurement technique. Inline ultrasonic flow sensors (shown in Figure 23**Figure 28**) (Model number ME PXN, Transonic Systems Inc., Ithaca, NY, USA) were used to measure the mitral and aortic flow rates. These flow sensors measure the difference of transit time of ultrasonic pulses propagating through the flow. This time difference is then used to measure the average velocity of the fluid

passing through the ultrasonic beam inside the pipe blocks. The figure and manufacture specifications are given below:

Figure 28: ME 25 PXN inline ultrasonic flow sensors (Transonic Systems Inc., Ithaca, NY, USA)

Specifications	
Sensor size	25 PXN
Tubing ID	25.4 mm
Barb OD	29.0 mm
Lower linear limit	10 L/min
Maximum measurement range	-100 to +100 L/min

Table 5: Manufacturer specifications for ME 25 PXN inline ultrasonic flow sensor (Transonic Systems Inc., Ithaca, NY, USA)

The flow rates measured using the inline ultrasonic flow sensors were displayed in real time on a console (T402-Series. Transonic Systems Inc., Ithaca, NY, USA). These consoles provide analog voltage output signals which goes through a low pass filter before being stored on a computer. Out of all the filters provided on the console (0.1, 10, 40, 160 Hz), 10 Hz was used during the experiment. The flow console figure and manufacturer specifications are shown below.

Figure 29: T402-Series Console (Transonic Systems Inc., Ithaca, NY, USA)

Specifications	
Flow Console Compatibility	ME-PXL & ME-PXN – series flow probes
Filters	0.1, 10, 40, 160 Hz
Voltage range	-5 to +5 volts
Output resistance	500 Ohm
Ultrasonic frequency range	600 KHz to 14.4 MHz

Table 6: Manufacturer specifications for T402-Series Console (Transonic Systems Inc., Ithaca, NY, USA)

3.6 Data acquisition system

NI USB-6251 DAQ (National Instruments Corporation, Austin, Texas, USA) board was used to record data from the above equipment using a standard BNC cable. Hemodynamic data (flow rate & pressures) were acquired using custom LabVIEW (National Instruments, Version 12.0f3) program. Figure and specifications for the Data acquisition instrumentation board system are shown below.

Figure 30: NI USB-6251 Data acquisition instrumentation board (National Instruments Corporation, Austin, Texas, USA)

Specifications	
Analog output channels	2
Analog input channels	8
Number of triggers	1
ADC resolution	16 bits
Sampling rate	1.00 MS/s multiple channel
Input voltage range	± 0.1 V to ± 10 V
Trigger source	APFI 0

Table 7: Manufacturer specifications for NI USB-6251 DAQ (National Instruments Corporation, Austin, Texas, USA)

3.7 Particle Image Velocimetry (PIV) system

2D planar, phase locked PIV was used to visualize intraventricular flow field in the current study. The setup consisted of following equipment:

1. Model DM30-527 diode-pumped, Nd:YLF Q-switched, single cavity green laser, maximum pulse energy of 30 mJ at 527 nm, pulse rate of 1-10 kHz (Photonics Industries International. Inc.)
2. An external laser controller which can regulate pulse power, frequency and the source input.
3. Kodiak Recirculating Chiller (Lytron Inc., Woburn, MA, USA) with cooling capacities of 825 W - 11 kW.
4. PMMA Fluorescent seed particles (1 – 20) microns, 532 nm excitation/584 nm emission.
5. DFM/M-E02 – Complete Kinematic Beam Turning 30 mm Cage Cube with Dielectric-Coated Right-Angle Mirror (Thorlabs Inc., Newton, New Jersey, USA).
6. Imager sCMOS camera, maximum resolution - 5.5 million pixel, spectral range - 370 – 1100 nm, read-out noise - <3 e-, pixel rate - 50 (286 MHz), CCD chip size - 2560 x 2160, CCD pixel size - 6.5 µm, exposure - 10 µs - 100 ms, e-pixel - 30 k, digital output - 16 bit (LaVision GmbH, Goettingen, Germany).
7. OG-550, 50mm Dia. Longpass Filter (Edmund Optics Inc., Barrington, NJ, USA).

Figure 31: PIV equipmet: A)Model DM30-527 laser and controller, B)Kodiak Recirculating Chiller, C)Fluorescent tracer particles, D)DFM/M-E02 right angle mirror, E)Imager sCMOS camera, and F)OG-550 Longpass Filter

CHAPTER IV

INSTRUMENT CALIBRATION

4.1 Calibration

Calibration is an essential procedure on measurement instrumentation in order to convert measurements from a known unit to a desired unit. Calibration was performed on pressure transducers to convert from volts to pressure in units of mm Hg, and on flow probes to convert from volts to flow rate in units of L/min. Linearity of the signal was assumed for both pressure transducers and flow probes and verified by checking the R^2value of linear regression trendlines. The methods used to calibrate the flow probes and pressure transducers are described in detail below.

4.1.1 Pressure transducer calibration

Deltran® Disposable Pressure Transducer was connected to the Delta-Cal™ Pressure transducer simulator/tester at the pneumatic port (see **Figure 26**B). Pressure was applied using the adjustable dial located on the opposite side of the pneumatic port in predetermined increments in between the range of -100 to +150 mmHg. Voltage produced by the excited strain gauge inside the transducer was amplified and measured at each individual point using a strain gage signal conditioner. These values were later plotted in order to get the slope from a linear trend line fitted to the data.

The standard uncertainty of the voltage readings acquired during this experiment was measured to be around 0.09%. The step-by-step procedure for calibrating the pressure transducer are given below:

1. Connect the Deltran® disposable pressure transducer to the appropriate channel on the signal conditioning module.
2. Connect the signal conditioning module to the data acquisition instrumentation board.
3. Connect the Deltran® disposable pressure transducer to the pneumatic port (shown in **Figure 26**B) on the Delta-Cal™ pressure transducer simulator/tester.
4. Turn the Delta-Cal™ pressure transducer simulator/tester on and also prime the Delta-Cal™ pressure transducer with the same fluid used in the flow loop.
5. Record the voltage with zero pressure in the system before beginning the calibration process.
6. Turn the adjustable dial (shown in **Figure 26**B) in counter clockwise direction until the pressure reaches the lower limit of the equipment range (-100 mmHg).
7. Record and save the pressure transducer output (voltage readings) using a LabVIEW (National Instruments, Version 12.0f3) program.
8. Increase the pressure of the system and record the output values simultaneously.
9. Repeat steps 7 and 8 for the entire operating pressure range for the Deltran® Disposable Pressure Transducer.
10. Stop the experiment when the final pressure reaches the upper limit of the operating pressure range.
11. Plot the recorded voltage values against pressure and calculate the slope for all the points.
12. This slope can then be used as a calibration constant for the Deltran® Disposable Pressure Transducer during the experiment.
13. Note that the calibration needs to be done for each individual pressure transducer separately.

As an example, the pressure used and voltage obtained during the calibration of a Deltran® Disposable Pressure Transducer are plotted in a graph shown below.

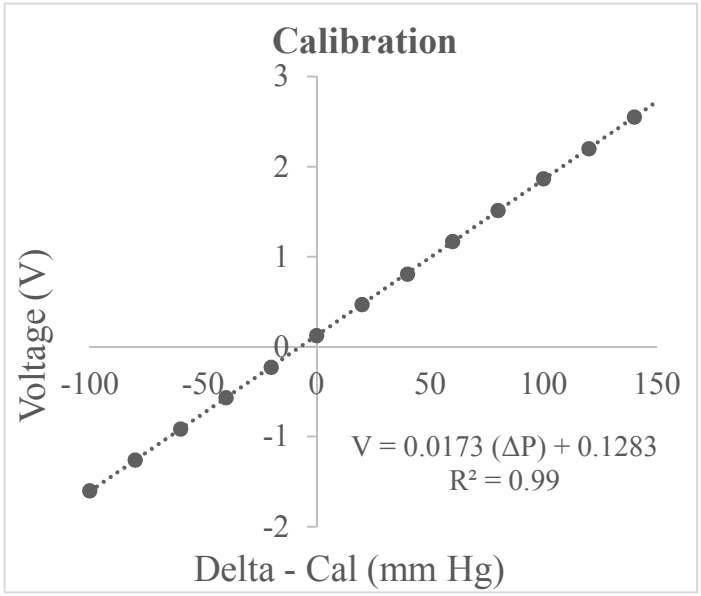

Delta-Cal™ Pressure transducer simulator (mm Hg)	Voltage readings (V)
-100	-1.60
-60	-0.91
-20	-0.23
0	0.13
20	0.47
60	1.17
100	1.87
140	2.56

Figure 32: Representative plot showing variation of voltage and pressure for pressure transducers used in the flow loop. A linear trend line was plotted to fit the data

4.1.2 Flow probe calibration

Transonic PXN inline ultrasonic flow probe was connected to a simple closed loop circuit (shown in

Figure 33) driven by a 1/12 HP submersible pump externally.

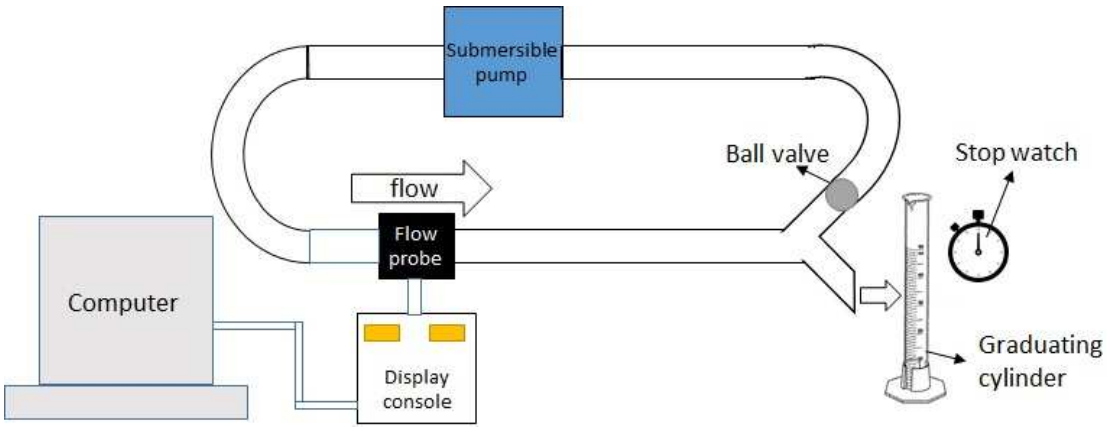

Figure 33: Detailed schematic of the flow loop used to calibrate flow probes

The above flow loop was operated in the range of 4 – 25 L/min flow rates for each flow probe separately. Voltage produced by the sensors were amplified by Transonic T400-series console and recorded at each individual point using the data acquisition instrumentation board. These values were later plotted in order to get the slope from a linear trend fitted to the data. The standard uncertainty of the voltage readings acquired during this experiment was measured to be around 0.14%. The step-by-step procedure for calibrating the ultrasonic flow probe is given below.

1. Connect the Transonic T400-Series Console to the data acquisition instrumentation board using standard BNC cable.
2. Turn the submersible pump on and prime the flow loop with the same fluid used in the experiment.
3. Record the voltage with zero flow in the system before beginning the calibration process.
4. Start the experiment at the lowest flow rate in the predetermined flow rate range mentioned earlier.
5. Record and save the output values from the ultrasonic flow probes (voltage readings) using a custom LabVIEW (National Instruments, Version 12.0f3) program.
6. Increase the flow rate of the flow loop to an appropriate value ($\Delta Q \approx 5$L/min) and record the output values simultaneously.

7. Repeat steps 5 and 6 until the flow rate reaches the upper limit of the predetermined flow rate range.
8. Plot the recorded voltage values against flow rate, perform linear regression on the data and calculate the slope for all the points.
9. This slope can then be used as a calibration constant for the flow sensors during the experiment.

As an example, the flow rates and voltage values obtained during the calibration of a Transonic PXN inline ultrasonic flow are plotted in a graph shown below.

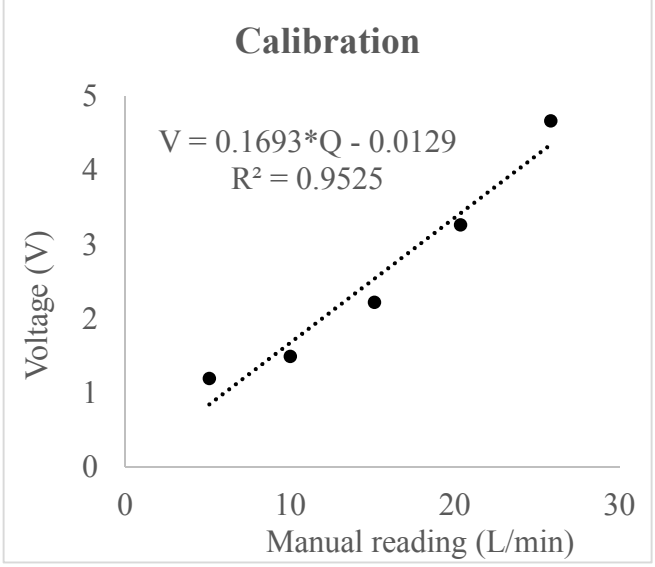

Manual reading (Q)	Voltage readings (V)
5.1	1.20
10	1.50
15.1	2.22
20.33	3.27
25.8	4.67

Figure 34: Variation of voltage (V) of sensor and measured flow rate (Q) plotted for the flow probe used in the flow loop

4.2 Stiffness Testing

The stiffness of various LV physical models used in this study were calculated using the equation (4) below.

$$\text{Compliance} = \frac{\Delta V}{\Delta P} \quad \{3\}$$

$$\text{Stiffness} = \frac{\Delta P}{\Delta V} \quad \{4\}$$

The step-by-step procedure for determining the stiffness of the LV physical models is given below. **Figure 35** shows the setup during the LV compliance testing.

1. Isolate the LV chamber including the physical model from the flow loop.
2. Keep the LV chamber exposed to the atmospheric pressure and seal the openings on the LV physical model externally.
3. Fill the physical model via the filling port shown in **Figure 35** with water-glycerin fluid used in the loop until the bag expands to its maximum capacity and measure the volume (ml).
4. Record and save the pressure inside the physical model using a custom LabVIEW (National Instruments, Version 12.0f3) program.

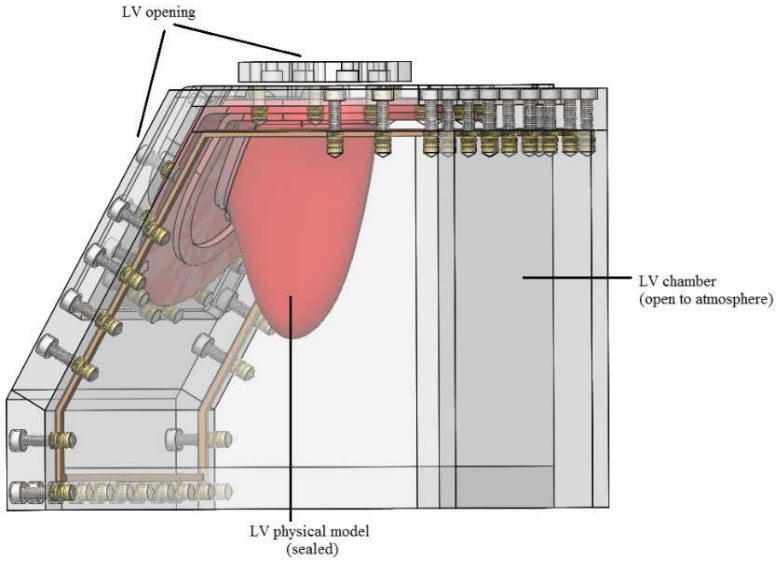

Figure 35: Isolated LV chamber and LV physical model during compliance testing

5. Add predetermined amount of fluid (ΔV) from the physical model.
6. Repeat steps 4 and 5 until the LV physical model reaches its maximum volume.
7. Plot the recorded values of pressure and volume for each model, perform linear regression on the data and calculate the slope for all the points.

	ΔP (mmHg)			
ΔV (ml)	**Model #1**	**Model #2**	**Model #3**	**Model #4**

225	131	138	141	NA
215	103.5	112	115	NA
205	76.6	85	89	NA
195	51.4	56	59	283.6
185	27	27	31	160
175	6.6	4	9	67

Table 8: ΔP and ΔV values for all the LV physical models used in the experiment

The LV stiffness of the physical models obtained using the above mentioned procedure are shown in

Table 8. The data points represent LV stiffness of the individual physical models and the linear trend among them. The stiffness of 4 physical models were measured using the protocol.

4.3 Waveform

The input waveform required by the pump was generated using a custom LabVIEW (National Instruments, Version 12.0f3) program (provided in the appendices). These are the following steps involved in making a waveform:

1. Enter the file path and specific input file name which is needed to be digitized.
2. Specify the input image format (JPEG, PNG, BMP)
3. Enter a file name for the output file path and select the spline option.
4. Select the origin on the loaded image.
5. Move the cursor to a specific part of the curve and include it into the interpolation. Number of points included into the interpolation should increase with increase in complexity of the curve.

Verify the curve and export the plot area into desired format (.txt, .dat, .rtf).

CHAPTER V

EXPERIMENTAL METHODS

5.1 Experimental Procedure

The LV chamber and the flow loop were first filled with the blood mimicking fluid (65% glycerin/vol. – 35% water/vol. mixture) and primed before starting the experiment. Windkessel elements inside the flow loop were tuned to get physiological conditions (shown in

Table 9) with the least stiff physical model inside the flow loop. The experiment starts by turning the programmable piston pump on and slowly increasing the amplitude. Hemodynamics data (flow rate and pressures) were recorded and saved on a computer using a LabVIEW (National Instruments, Version 12.0f3) program. The experiment was later repeated for LV physical models of increasing wall stiffness while maintaining the LV chamber pressure, compliance fluid level, resistance, reservoir fluid level, pump amplitude, and input waveform constant and similar to the values used for least stiff model.

Hemodynamics	
Aortic pressure	120/80 mm Hg
Average CO (Peak Mitral and Aortic flow rates)	5 L/min (15 L/min & 25 L/min)
Heart rate	70 bpm
Stroke volume	70-75 mL

Table 9: Physiological hemodynamic characteristics observed in normal adult circulation.

5.2 Particle image velocimetry Procedure

The PIV setup used in the current experiment and the schematics are shown in the **Figure 36**. The fluid inside the LV physical model was homogeneously seeded using (seeding particle mentioned earlier). The laser beam generated from the single head double-pulsed solid-state laser was steered using mirrors and transformed into a sheet using a cylindrical lens. This 2 mm thin laser sheet is passed through the center plane of the LV model which illuminates the tracer particles inside his volume. The illuminated laser sheet was adjusted such that it encloses the entire LV physical model in its FOV (field of view). Spatial calibration was performed on the LV center plane using a 2D target plate fixed to a retort stand. In order to improve the signal quality, a black poster board was used behind the LV chamber. Laser pulse separation (*dt*) in the range of 1200 – 1500 µs was used across all time points in the diastolic period of the cardiac cycle. Images were acquired by Imager sCMOS camera equipped with Nikon AF Micro-Nikkor 60 mm lens. These closely spaced laser pulses yielded image pairs during each cardiac cycle which was later processed to evaluate fluid properties. Lens aperture was setup to f/2.8 (Maximum Aperture) to maximize the intensity of the light scattered by the seeding particles. The field of view (FOV) during the experiment was measured to be around 9 cm in length and 6 cm in diameter. This process was repeated at multiple reference points throughout the entire diastole (shown in **Figure 37**) for 200 cardiac cycles.

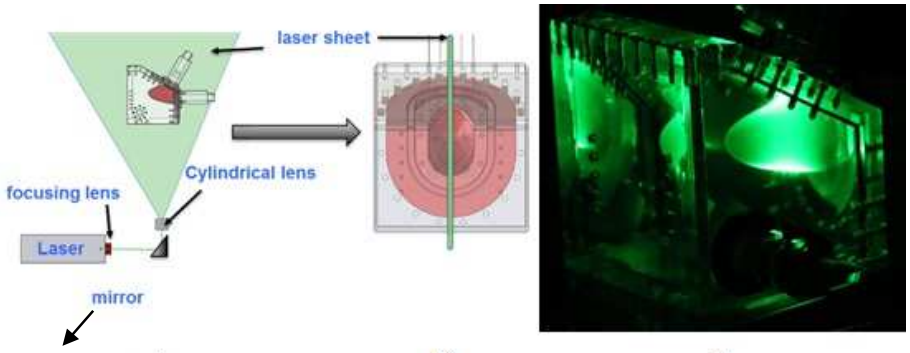

Figure 36: A) Schematics of the PIV setup (side view). B) Laser sheet passing through the center plane of the physical model (front view). C) Illuminated LV physical model during the experiment

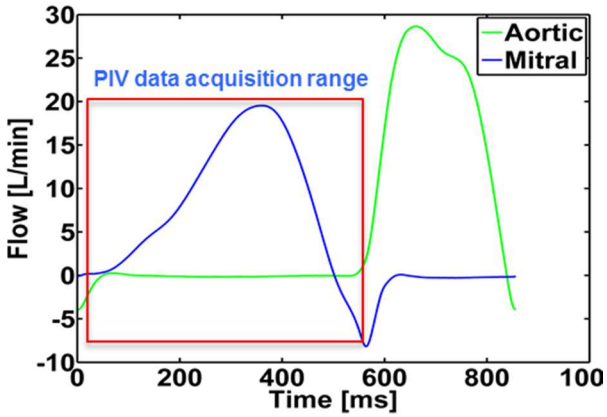

Figure 37: Phase-locked 2D PIV data acquisition range in the highlighted region (diastole). Total of 35 phase-locked points were acquired

The raw PIV image pairs were processed using DaVis 8.2.4 (LaVision GmbH, Goettingen, Germany) which divides the raw image (shown in **Figure 38**) into small subsections called "interrogation regions". The resultant velocity vector between two images in an image pair are determined using cross-correlation for each interrogation region (IR). The resultant velocity inside each IR with respect to the image pairs is calculated using the time delay (dt) mentioned earlier.

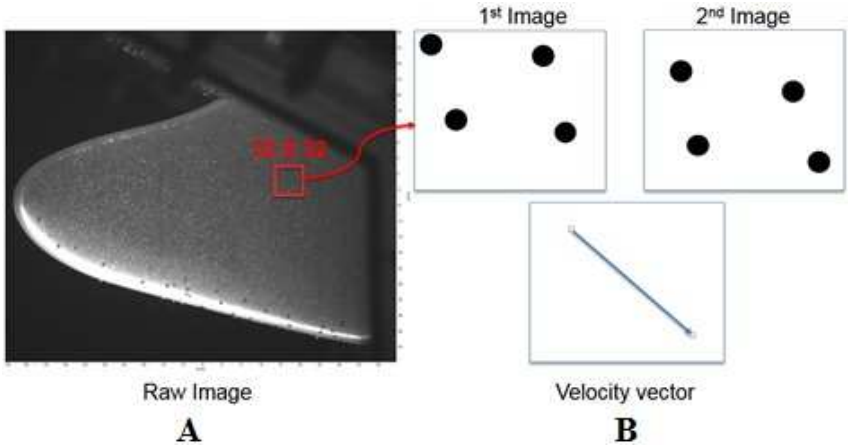

Figure 38: A) Raw image acquired by the Imager sCMOS camera during PIV. B) Shows raw image pair divided into user specified interrogation windows (in this case 32 X 32 pixel) which is later processed by DaVis 8.2.4 (LaVision GmbH, Goettingen, Germany) to obtain velocity vectors

Pre-processing was done by performing sliding background subtraction of a scale length of 5 pixels and masking (shown in **Figure 39**) the Area of Interest (AOI). Multi-pass with cross-

correlation decreasing IR size (64 X 64 pixels with 50% overlap, 2 passes → 32 X 32 pixels with 50% overlap, 3 passes) was used to process these image pairs (see **Figure 39**).

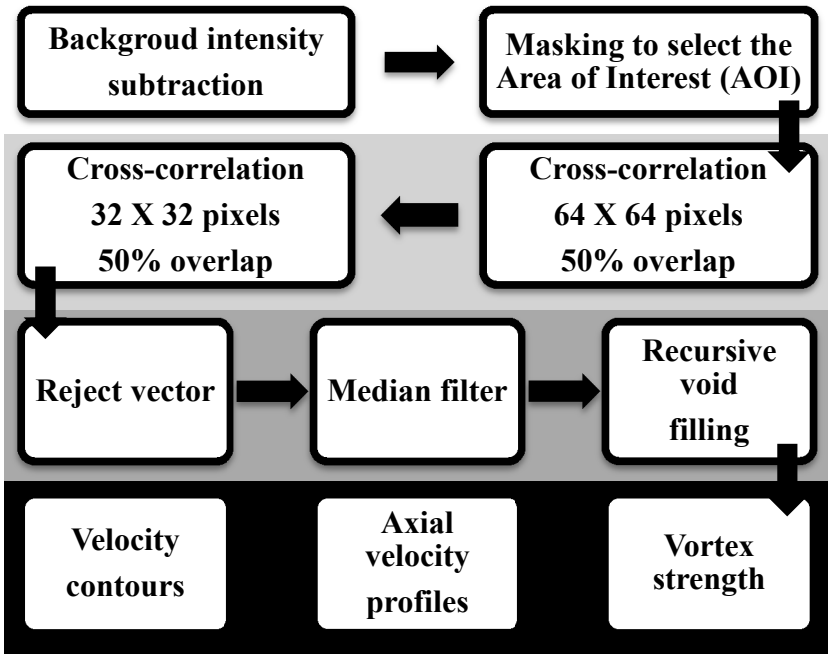

Figure 39: Algorithm shows the step by step procedure followed during PIV pre and post-processing

Post-processing was done by rejecting vector (if the signal to noise ratio < 1.2), applying optimal smoothing, a median filter in order to eliminate outliers and using recursive filling of voids in the vector field. Ensemble averaging of 200 image pairs for each phase-locked data points was performed, resulting in a single data file for each data point. (LOOK AT IKAY AND DR.S PAPER AND INCLUDE CALCULATION OF ERRORS RELATED TO PIV MEASUREMENT)

5.2.1 PIV Uncertainty

PIV data processing involves instruments and chains of algorithm coupled with uncertainty sources applied to the image pairs acquired. Almost all the time results come with the expense of measurement error, which is unknown. An estimate of an interval containing error can be produced using uncertainty quantification. For this particular experiment, the uncertainty standard deviation of the velocity was calculated to be around 0.004 m/s using DaVis 8.2.4

(LaVision GmbH, Goettingen, Germany). The confidence level of the data was found to be 68.5% with 1σ, assuming a Gaussian distribution.

While data processing, cross-correlation functions were used which are usually associated with errors like signal to noise ratio (SNR). One of the measure of SNR is the primary peak ration (PPR), which is defined as the ratio between the first tallest to the second tallest correlation peak. In the previous studies concerned with PIV, PPR was used as a method to detect real displacement [85, 86]. Uncertainty (U) [87]of the displacement magnitude using PPR (quantified using DaVis 8.2.4. LaVision GmbH, Goettingen, Germany) was calculated to be 0.15 which is given by equation (5) shown below,

$$\mathrm{U} = 0.7 * PPR^{-1.62} \qquad \{5\}$$

5.3 Calculated Quantities

This subsection will provide the definition of quantities calculated like velocity profiles, vortex strength, kinetic energy, and dissipation rate from hemodynamics and PIV data.

5.3.1 Velocity profiles

The inflow jet characteristics during diastole were quantified using 2D velocity profiles. Specifically, the radial (septal-lateral axis, r-direction) variation of axial velocity u (in apical-basal axis direction) was examined. **Figure 44** shows the coordinate system (x, r) along the LV model here. The axial stations were chosen in integral increments ofd_0, which represents the diameter of the mitral BMHV (Regent™, St. Jude Medical, Inc., St. Paul, MN, USA).

5.3.2 Circulation

LV vortex ring formed during diastole was identified by applying swirling strength criterion (λ_{ci}) with a threshold of 4.2% of the local maximum value [71, 88, 89]. Swirling strength criterion (λ_{ci}) is defined as the imaginary part of the complex eigenvalues of the velocity gradient tensor, tensor,∇U. Mathematically, λ_{ci} for 2D PIV data can be calculated using the equation (6) shown below,

$$\lambda_{ci} = \mathrm{Im}[\mathrm{eig}(\nabla U)] = \frac{1}{2}\left[\sqrt{\left(\frac{du}{dx} - \frac{dv}{dy}\right)^2 + 4.\frac{du}{dy}.\frac{dv}{dx}}\right] \quad \{6\}$$

After the identification, the strength of the vortex ring anterior to the LV was then calculated using the Stokes theorem for circulation (Γ). Mathematically, (Γ) is shown by the equation (7) below,

$$\Gamma = \int_0^A \omega_z dA = \sum_A \omega_z dxdy \quad \{7\}$$

In the above equation, ω_z represents the z-axis (out-of-the plane) vorticity, *A* represents the area of a closed region of the vortex selected to be examined from the swirling strength criterion.

5.3.3 Kinetic energy

Kinetic energy of the flow field in diastole plays an important role in preparing for systolic ejection of blood through the aorta, and is directly related to the CO. In this study, kinetic energy per unit mass across the LV chamber is calculated using the equation (8) shown below,

$$\mathrm{K.E.} = \int_0^A \frac{1}{A}\left(\frac{u^2 + v^2}{2}\right) dA = \sum_A \left(\frac{u^2 + v^2}{2}\right) dxdy \quad \{8\}$$

Here, '*u*' and '*v*' represents instantaneous velocities inside the LV chamber, whereas, *A* represents the area of the LV field of view.

5.3.4 Energy dissipation rate

Previous studies have shown that energy dissipation rate (EDR) is dependent on the size and shape of the vortex ring inside the LV [43]. The equation used to calculate EDR from 2D PIV data is given by the equation (9) shown below,

$$\emptyset = \nu\left[2\left(\frac{du}{dx}\right)^2 + 2\left(\frac{dv}{dy}\right)^2 + 2\frac{du}{dy}\frac{dv}{dx} + \left(\frac{du}{dy}\right)^2 + \left(\frac{dv}{dx}\right)^2\right] \quad \{9\}$$

Here, '$\emptyset$' is the energy dissipation rate, 'ν' represents the kinematic viscosity of the fluid, $\frac{du}{dx}$, $\frac{dv}{dy}$, $\frac{du}{dy}$, $\frac{dv}{dx}$ are 2D velocity gradients.This chapter helps us understand the effects of LV wall

stiffness on the filling fluid dynamics with and without the presence of A-wave at a constant heart rate of 70 BPM. A total of 2 experiments among 3 LV physical models of varying LV wall stiffness were conducted in this study. The following sections are a visual representation of hemodynamics, velocity field, velocity profile, vortex strength, and energetics.

CHAPTER VI

RESULTS

This chapter helps us understand the effects of LV wall stiffness on the filling fluid dynamics with and without the presence of A-wave at a constant heart rate of 70 BPM. A total of 2 experiments among 3 LV physical models of varying LV wall stiffness were conducted in this study. The following sections are a visual representation of hemodynamics, velocity field, velocity profile, vortex strength, and energetics.

6.1 Hemodynamics

Hemodynamics is a study of blood flow which explains the physical laws that govern the movement of blood inside the blood vessels. A clear understanding of cardiac hemodynamics is essential in order to diagnose and treat possible cardiac malfunctions. Aortic pressure, flow rate, and stroke volume are the most basic and important hemodynamic parameters in a human cardiovascular system. Flow rate is defined as the rate of blood flow through the heart in a minute, whereas, stroke volume is defined as the amount of blood being pumped in a single stroke. These repeated strokes leads to systemic contraction and relaxations of the heart which create necessary blood pressure inside the arteries, varying between (systolic) maximum and (diastolic) minimum values of pressure. On an average, human beings exhibit an arterial blood

pressure of 120/80 mmHg, flow rate of 5 L/min and a stroke volume of 70-75 mL at a constant heart rate of 70 BPM. In this study, hemodynamic data was acquired over 200 cardiac cycles simultaneously with the PIV data and ensemble averaged using a custom MATLAB code. The hemodynamic data for both cases (with and without A-wave) were analyzed and documented in the tables shown below. A close observation of these tables show that the hemodynamic trend among LV physical models of varying stiffness does not change with or without A-wave. **Table 11** shows the final ensemble averaged hemodynamic data compared against LV wall stiffness with the absence of A-wave. The table clearly shows a strong decreasing trend in aortic pressure (discussed in detail below), LV pressure (LVP), cardiac output (CO), Peak mitral and aortic values (discussed in detail below), diastolic time period, E-wave deceleration time, stroke volume (SV), end-diastolic volume (EDV) and ejection fraction (EF) with the increase in LV stiffness.

Stiffness [mm Hg/mL]	**1.64**	**2.15**	**8.48**
Aortic pressure [mm Hg]	122/79	89/50	79/43
LVP [mm Hg]	133/-23	106/-16	93/-10
Average Flow rate [L/min]	4.9	3.8	2.9
Peak Mitral inflow [L/min]	15.2	13.4	11.8
Peak Aortic outflow [L/min]	28	24.18	22
E-wave duration in diastole [ms]	556	486	428
Deceleration time [ms]	207	155	110
Stroke volume [mL]	70.1	58.6	54.2
End-diastolic volume (EDV)	121	111	106
EF [%]	**58%**	**53%**	**51%**

Table 10: Ensemble averaged hemodynamic data compared amongst LV physical models of different LV wall stiffness with the absence of A-wave

Table 11 shows the final ensemble averaged hemodynamic data compared against LV wall stiffness with the presence of A-wave. Similar to that of **Table 10**, the aortic pressure (discussed in detail below), LVP, CO, Peak mitral and aortic values (discussed in detail below),

diastolic time period, E-wave deceleration time, SV, EDV and EF dropped whereas, the E/A ratio and A-wave duration went up significantly with the increase in LV stiffness.

Stiffness [mm Hg/mL]	**1.64**	**2.15**	**8.48**
Aortic pressure [mm Hg]	123.7/75	102/62	89/40
LVP [mm Hg]	152/-75	110/-40	108/-43
Average Flow rate [L/min]	5.3	4.5	4
Peak Mitral inflow [L/min]	15.67	14.36	13.93
Peak Aortic outflow [L/min]	24.8	18.7	17.6
E-wave duration in diastole [%]	74%	59%	58%
A-wave duration in diastole [%]	26%	41%	42%
Diastolic duration [ms]	567	541	502
E/A ratio	1.2	1.7	2.2
Deceleration time [ms]	159	125	116
Stroke volume [mL]	78.5	64	58
End-diastolic volume (EDV)	125	118	115
EF [%]	63%	54%	50%

Table 11: Ensemble averaged hemodynamic data compared amongst LV physical models of different LV wall stiffness with the presence of atria systole

Aortic pressure and mitral flow curves were discussed in detail and plotted as a function of varying LV wall stiffness (mmHg/mL) over a single cardiac cycle (856 milliseconds) at a heart rate of 70 BPM in the sections below. Each individual curve shown in **Figure 40 – 38** corresponds to a unique LV wall stiffness (mmHg/mL) which are represented in a legend.

6.1.1 Aortic pressure

The total pressure inside the aorta was measured instantaneously using Deltran® Disposable Pressure Transducer (**Figure 26**A) (Model number: DPT-200. Utah Medical Products Inc., Midvale, UT, USA), located downstream of the aortic valve inside the outflow tract. The initial phase of the graph shows a continuous drop in the aortic pressure during diastole followed by a sharp peak which indicates the beginning of systole. The minimum value attained before the

peak corresponds to the arterial pressure during relaxation. Whereas, the peak value corresponds to the pressure inside the arteries during contraction. Both figures show a periodic signal with a consistent profile of the signal between three LV physical models used in this study.

A) Aortic pressure curve (absence of A-wave)

Figure 40 shows aortic pressure plotted as a function of varying LV wall stiffness with the absence of A-wave. The graph shows LV physical model with least stiffness (1.64 mmHg/mL) exhibiting physiological aortic pressure (122/79 mmHg). Meanwhile, LV physical models with increased wall stiffness (2.15 mmHg/mL, 8.48 mmHg/mL) display reduced aortic pressures (89/50 mmHg, 80/43 mmHg). This plot also shows a slight decrease in ΔP (Systolic/diastolic pressure) value from least stiff (ΔP = 43 mmHg) to most stiff (ΔP = 37 mmHg) LV physical model.

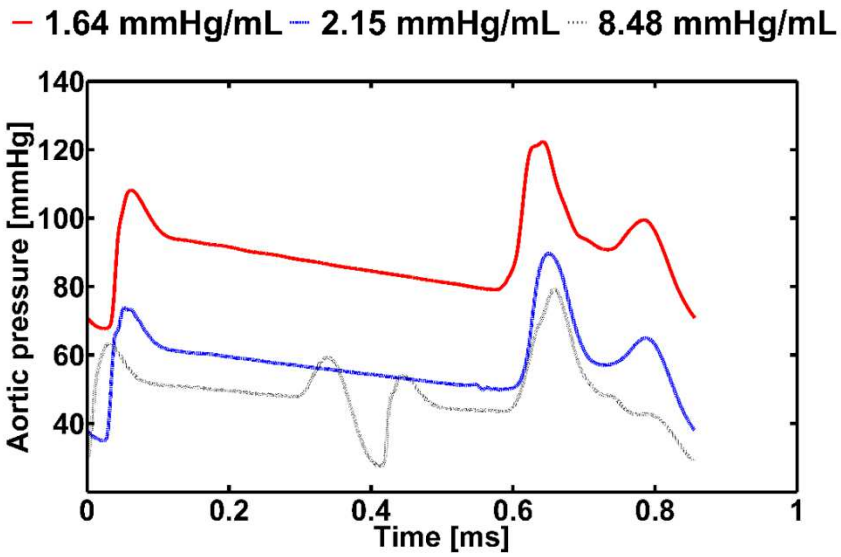

Figure 40: Aortic pressure plotted as a function of varying LV wall stiffness during a single cardiac cycle with the absence of A-wave

B) Aortic pressure curve (presence of A-wave)

Figure 41 shows aortic pressure plotted as a function of varying LV wall stiffness with the presence of A-wave. Like the previous plot, the LV physical model with least stiffness (1.64 mmHg/mL) displayed physiological aortic pressure (121/76 mmHg). Meanwhile, LV physical models with increased wall stiffness (2.15 mmHg/mL, 8.48 mmHg/mL) showed reduced aortic

pressures (100/60 mmHg, 81/49 mmHg). This plot showed a drop in ΔP (Systolic/diastolic pressure) value from least stiff (ΔP = 45 mmHg) to most stiff (ΔP = 32 mmHg) LV physical model similar to the **Figure 40**.

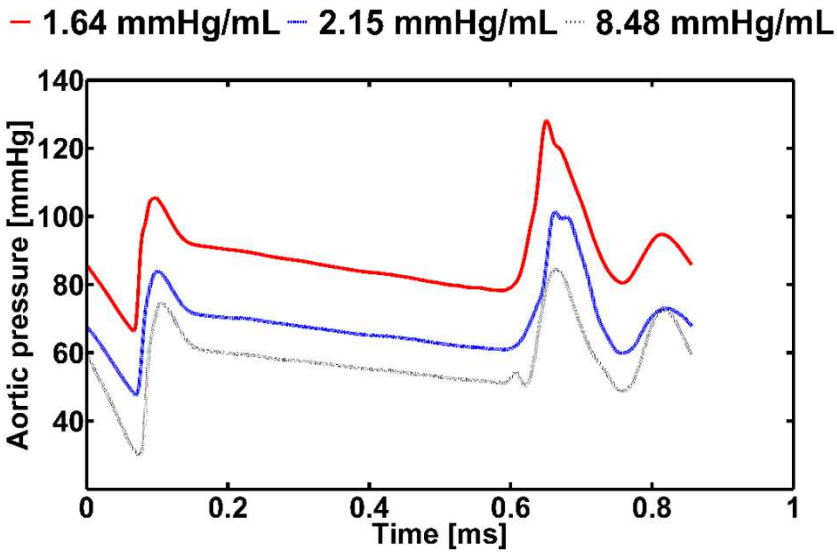

Figure 41: Aortic pressure plotted as a function of varying LV wall stiffness during a single cardiac cycle with the presence of A-wave

5.1.2 Flow rate

The rate of blood flow through the inflow and out flow tracts was measured using two Inline ultrasonic flow sensors (**Figure 28**) (Model number ME PXN. Transonic Systems Inc., Ithaca, NY, USA), located upstream of the mitral valve and downstream of the aortic valve. During ventricle relaxation, the flow curves starts increasing from zero/no flow value until it reaches the first peak, also known as E-wave. A second peak, also known as A-wave occurs immediately after the E-wave which ends in a negative peak called as closing volume. During the absence of A-wave, E-wave decelerates continuously until it reaches the closing volume. Both figures show a periodic signal with a consistent profile of the signal between three LV physical models used in this study.

A) Mitral flow curve (absence of A-wave)

Figure 42 shows the changes in instantaneous flow rate inside the LV plotted as a function of varying LV wall stiffness with the absence of A-wave. The mitral flow curve graph shows E-

wave only due to the absence of A-wave as described above. This plot shows LV physical model with least stiffness (1.64 mmHg/mL) exhibiting physiological mitral flow rate of 15.3 L/min. Meanwhile, LV physical models with increased wall stiffness (2.15 mmHg/mL, 8.48 mmHg/mL) display reduced mitral flow rates, 13.4 L/min and 11.8 L/min respectively. A comparison between these plot reveal that, the diastolic time period (Beginning of the E-wave until peak closing volume) reduced from least stiff (Dt = 556 milliseconds) to most stiff (Dt = 421 milliseconds) LV physical model.

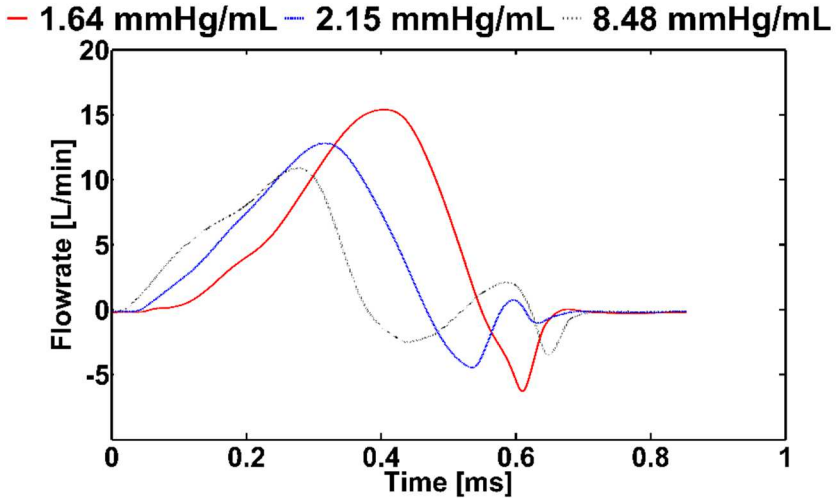

Figure 42: Flow rate plotted as a function of varying LV wall stiffness during a single cardiac cycle with the absence of A-wave

B) Mitral flow curve (presence of A-wave)

Figure 43 shows the changes in instantaneous flow rate inside the LV plotted as a function of varying LV wall stiffness with the presence of A-wave. This mitral flow curve graph shows both E-wave and A-wave due to the presence of A-wave. Like the previous plot, the LV physical model with least stiffness (1.64 mmHg/mL) displayed physiological mitral flow rate of 15 L/min (E/A = 1.2). Meanwhile, LV physical models with increased wall stiffness (2.15 mmHg/mL, 8.48 mmHg/mL) showed mitral flow rates with increased E/A ratios, 15 L/min (E/A = 1.7) and 15 L/min (E/A = 2.2) respectively. This plot also shows a reduced diastolic time period (Beginning of the E-wave, including A-wave until peak closing volume) from least stiff (Dt = 567 milliseconds) to most stiff (Dt = 502 milliseconds) LV physical model similar to **Figure 42**.

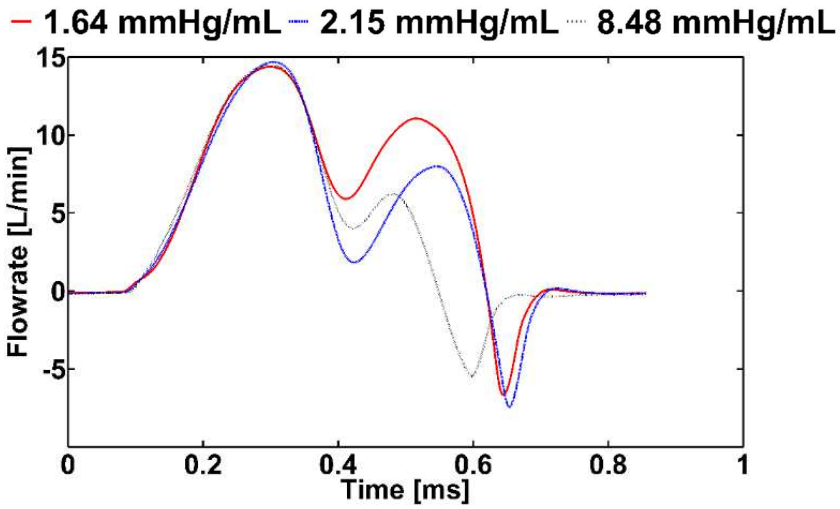

Figure 43: Flow rate pressure plotted as a function of varying LV wall stiffness during a single cardiac cycle with the presence of A-wave

6.2 Basic flow field

The raw images acquired by PIV were processed using DaVis 8.2.4 (LaVision GmbH, Goettingen, Germany) software. 2D velocity (m/s) field overlapped on to the z-axis vorticity (m^2/s) over the entire LV field of view (FOV) at different phases of cardiac cycle were plotted using Tecplot 360 EX 2015 R2 (Tecplot, Bellevue, WA, USA). The vectors displayed in these plots are called velocity vectors, which indicates the pace of the flow and its direction at a particular instant. These velocity vectors vary in length which are directly proportional to the velocity magnitude associated with that particular spatial location in the FOV. Column wise comparison of these plots in the table shows the flow development inside the LV during a single cardiac cycle. Meanwhile, row wise comparison shows the effects of LV wall stiffness on LV hemodynamics at a given phase of the cardiac cycle.

A) Velocity field overlapped on vorticity (absence of A-wave)

Table 12 shows a typical 2D inlet jet velocity field distribution overlapped onto vorticity measured using the PIV as a function of varying LV wall stiffness with the absence of A-wave. Among column wise comparison, we can see that in the LV physical model with lowest stiffness (1.64 mmHg/mL) the cardiac cycle starts from zero velocity with no vortex ring ($\omega_z = 0s^{-1}$) inside the LV (A). The inflow jet then reaches its highest velocity at peak E-wave (0.58 m/s)

forming a strong vortex ring (ω_z= -212.6s^{-1}) simultaneously (B). During E-wave deceleration, the size of the vortex ring and vorticity (ω_z= -230.2s^{-1}) increases whilst the velocity magnitude (0.51 m/s) drops (C). As the cardiac cycle reaches peak closing volume, the inflow jet disappears completely while the vortex ring attains its biggest size (26 mm) and lowest vorticity (ω_z= -45.2s^{-1}). In the row wise comparison, we can see that there is no variation in the first row. The 2nd and 3rd row however show a reduction in peak velocity magnitude (0.45 m/s → 0.33 m/s) and vorticity (ω_z= -208.6s^{-1} → ω_z= -141.6s^{-1}, ω_z= -135.0s^{-1} → ω_z= -72.6s^{-1}) with the increase in stiffness. The 4th row displays similar trend wherein the size of the vortex ring during peak closing volume decreases (24 mm → 21 mm) the increase in stiffness.

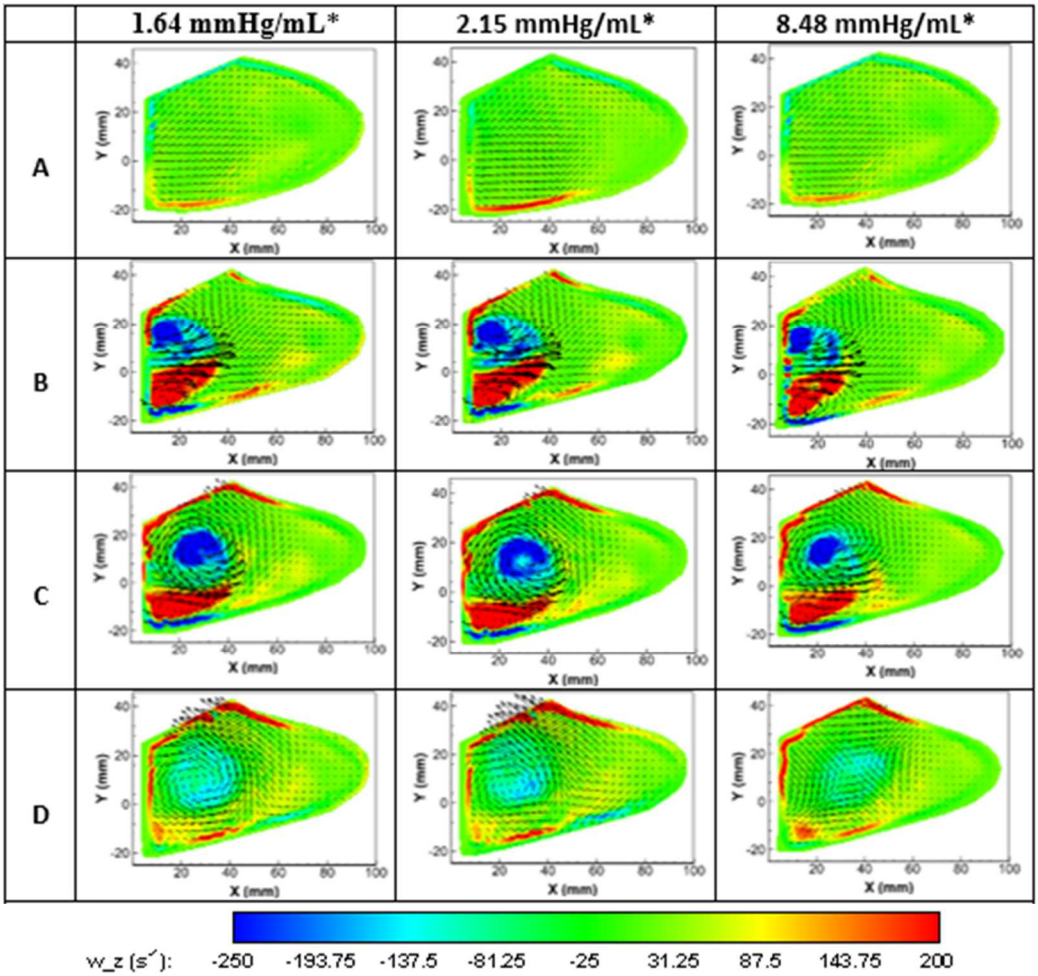

Table 12: 2D velocity field overlapped on vorticity during the presence of A-wave; A) Acceleration phase, B) Peak E-wave, C) Deceleration phase, and D) Peak closing volume

B) Velocity field overlapped on vorticity (presence of A-wave)

Table 13 shows a 2D inlet jet velocity field distribution overlapped onto vorticity measured using the PIV as a function of varying LV wall stiffness with the presence of A-wave. Similar to that of earlier table, column wise comparison shows that the LV physical model with lowest stiffness (1.64 mmHg/mL) starting its cardiac cycle from zero velocity with no vortex ring (ω_z= $0s^{-1}$) inside the LV (A). The mitral flow curve then begins accelerating during which a partial inlet jet is observed near the mitral valve of the LV (B). At C, the inlet jet reaches its 1st highest velocity at peak E-wave (0.5 m/s) forming a strong vortex ring (ω_z= -110.8 s^{-1}) simultaneously.

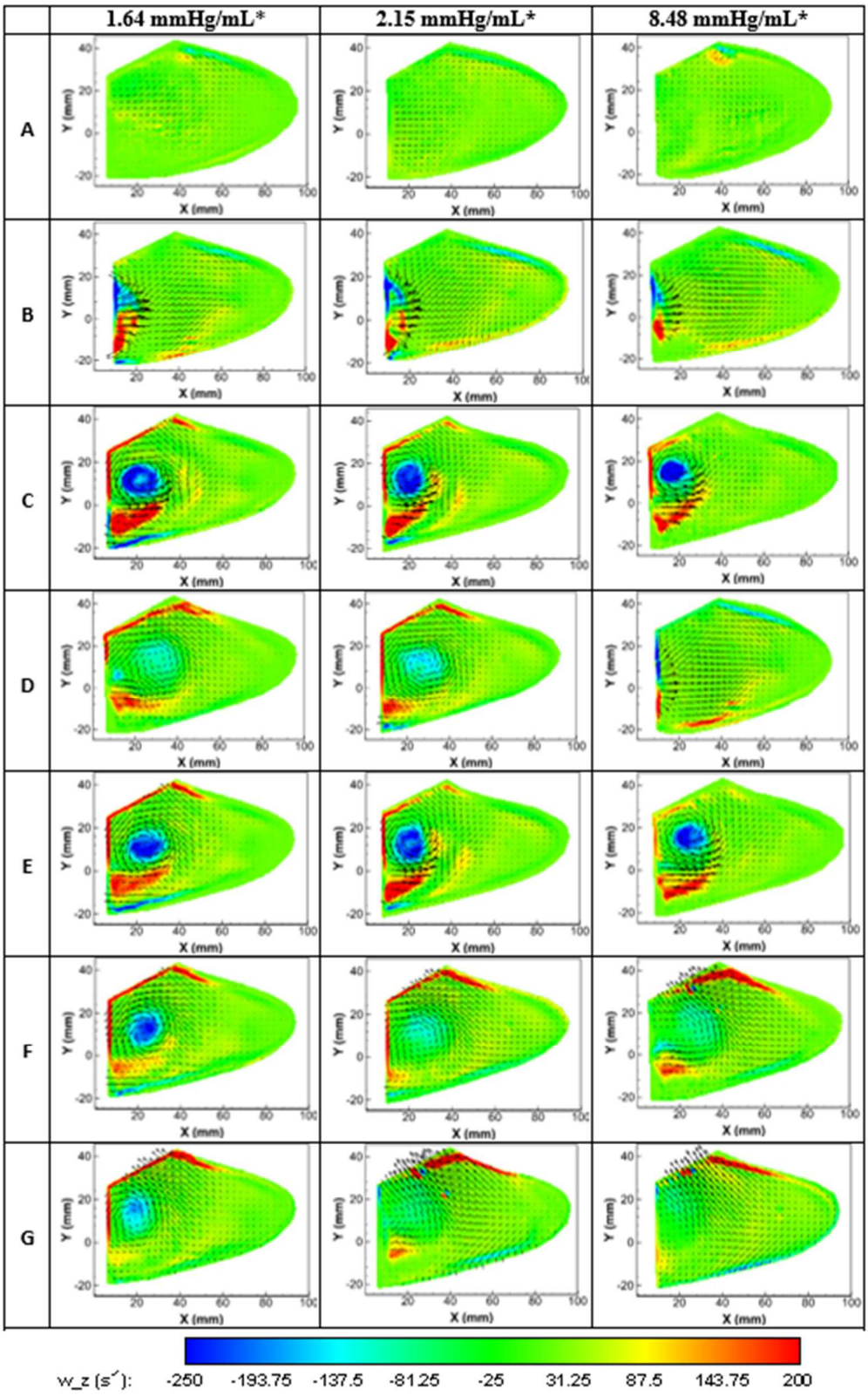

Table 13: 2D velocity field overlapped on vorticity during the presence of A-wave; A)Zero flow, B)Acceleration phase, C) Peak E-wave, D) Diastasis, E) peak A-wave, F) Deceleration phase, and G) Peak closing volume

During diastasis (D), the E-wave decelerates, causing the inlet jet to disappear partially meanwhile increasing the size of the vortex ring and reducing the vorticity (ω_z= -50.4 s^{-1}). At E, the inlet jet reaches its 2nd highest velocity at peak A-wave (0.45 m/s) which increases the vorticity of the LV vortex ring (ω_z= -168.3 s^{-1}) again. Deceleration of A-wave occurs immediately after mitral flow curve reaches the 2nd peak, which causes the inlet jet to completely vanish while the LV vortex ring keeps increasing (F). Diastolic phase ends as the mitral flow curve reaches its peak negative value (closing volume) at G, at which the LV vortex attains its maximum diameter (29 mm) before the beginning of systole.

The first row in the row wise comparison shows, no variation in the flow structure amongst all three LV physical models. The 2nd row shows, occurrence of partial inlet jet being delayed with the increase in LV wall stiffness. 3rd row shows a slight decrease in peak inlet velocity (0.46 m/s → 0.4 m/s) and vorticity (ω_z= -102.2s^{-1} → ω_z= -100.6s^{-1}). In the 4th row, decreased diastolic duration was observed during which, the stiffest LV physical model (8.48 mmHg/mL) showed earlier A-wave acceleration. The peak A-wave phase in the 5th row shows a similar trend wherein a slight decrease in velocity magnitude (0.4 m/s → 0.35 m/s) and vorticity (ω_z= -136.6 s^{-1} → ω_z= -112.6s^{-1}) with the increase in stiffness were observed. In row 6, the decrease in diastolic period is clearly visible, here the stiffest 2 LV physical models (2.15 mmHg/mL and 8.48 mmHg/mL) show no signs of LV vortex ring. In the last row, a weak vortex was observed in the least stiff model (1.64 mmHg/mL) whereas, the other 2 LV physical models showed signs of systole inside the LV.

6.3 Inflow jet characteristics

The spatial variation of velocity (m/s) vectors measured at four different locations ($^{x}/_{d_0} = 0, 0.5, 1, 1.5$) were compared with respect to the LV wall stiffness (mmHg/mL) at different phases of the cardiac cycle. Column wise comparison of these plots shows the fluid development inside the LV during a single cardiac cycle. Meanwhile, row wise comparison

shows the effects of LV wall stiffness on LV hemodynamics at a particular phase of the cardiac cycle. A close observation of these plots shows the effects of LV wall stiffness on structure, magnitude and evolution of the velocity vectors inside the LV physical model.

A) X-axis stations

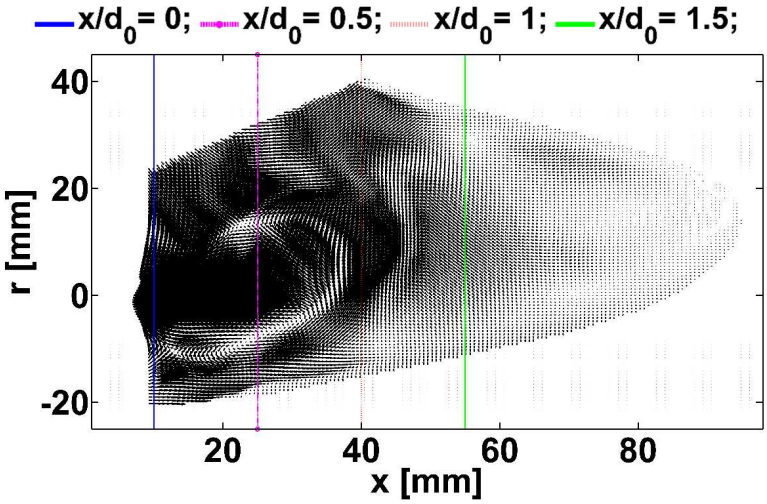

Figure 44: Vertical lines show the physical location of four different x-axis stations with respect to the LV physical model at which velocity profiles were plotted

B) Velocity profiles (absence of A-wave)

Table 14 shows 2D velocity profiles at $^{x}/_{d_0} = 0, 0.5, 1, 1.5$ in the XY-plane with the absence of A-wave. In the first column we see the inlet jet developing at $^{x}/_{d_0} = 0$ until it reaches peak velocity (0.58 m/s). As the cardiac cycle progresses into deceleration, the inlet jet moves deeper in to the LV which can be seen at $^{x}/_{d_0} = 0.5$. At the end of diastole (closing volume) the inlet jet disappears completely. Meanwhile, the anterior vortex inside the LV increases in size until it attains its largest diameter which can be seen in the lower right quadrant of the plots. The row wise comparison however shows a standard trend which denotes decrease in the inlet jet magnitude and LV anterior vortex size inside the LV with the increase in stiffness (2.15 mmHg/mL, 8.48 mmHg/mL).

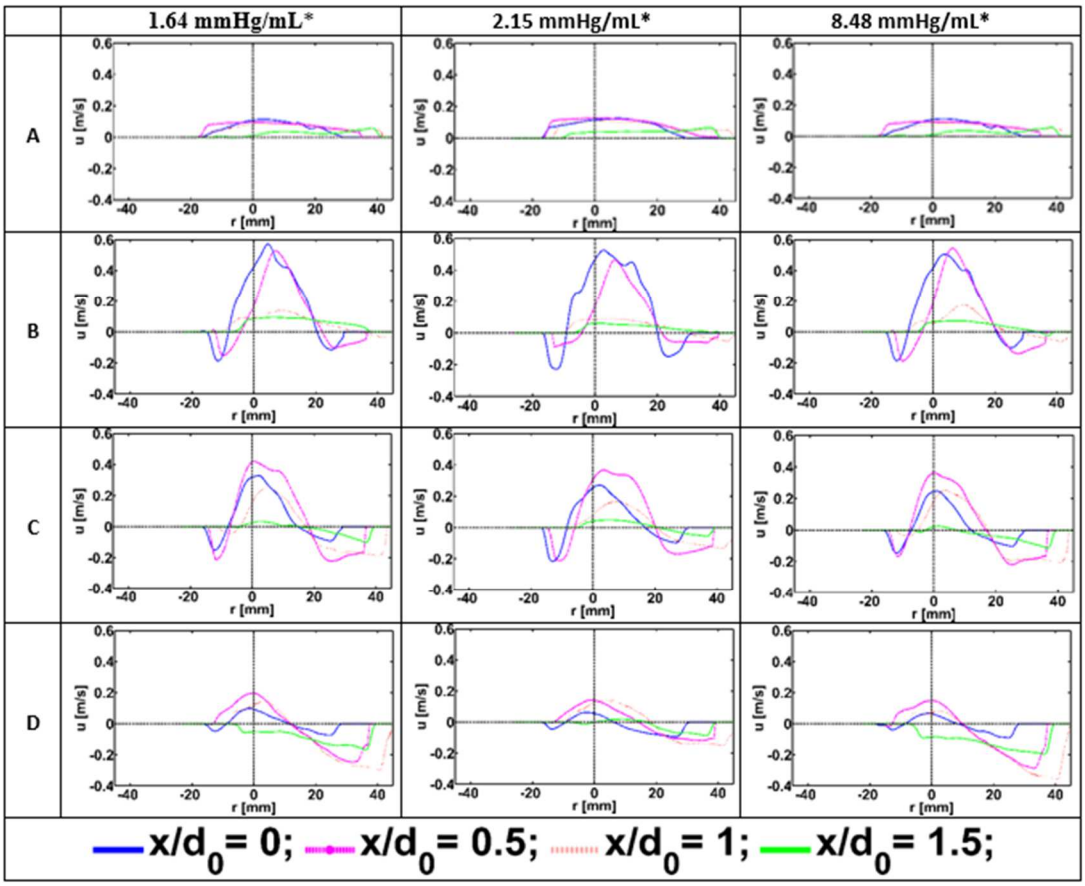

Table 14: 2D Velocity profile downstream of the mitral valve at x/d_0 = 0, 0.5, 1, and 1.5 during the absence of A-wave; A) Acceleration phase, B) Peak E-wave, C) Deceleration phase, D) Peak closing volume

C) Velocity profiles (presence of A-wave)

Table 15 shows 2D velocity profiles at $^{x}/_{d_0} = 0, 0.5, 1, 1.5$ in the XY-plane with the presence of A-wave. Similar to that of previous table, the first column shows the inlet jet developing at $^{x}/_{d_0} = 0$ until it reaches peak velocity (0.51 m/s) at peak E-wave. As the cardiac cycle enters diastasis the inlet jet decreases in magnitude while the LV vortex keeps growing. At peak A-wave, we can see the inlet jet rising again. At the end of diastole (closing volume) the inlet jet disappears completely. Meanwhile, the anterior vortex inside the LV increases in size until it attains its largest diameter which can be seen in the lower right quadrant of the plots. The row wise comparison shows a similar trend wherein the inlet jet magnitude and LV anterior vortex size decreases with increasing stiffness (2.15 mmHg/mL, 8.48 mmHg/mL).

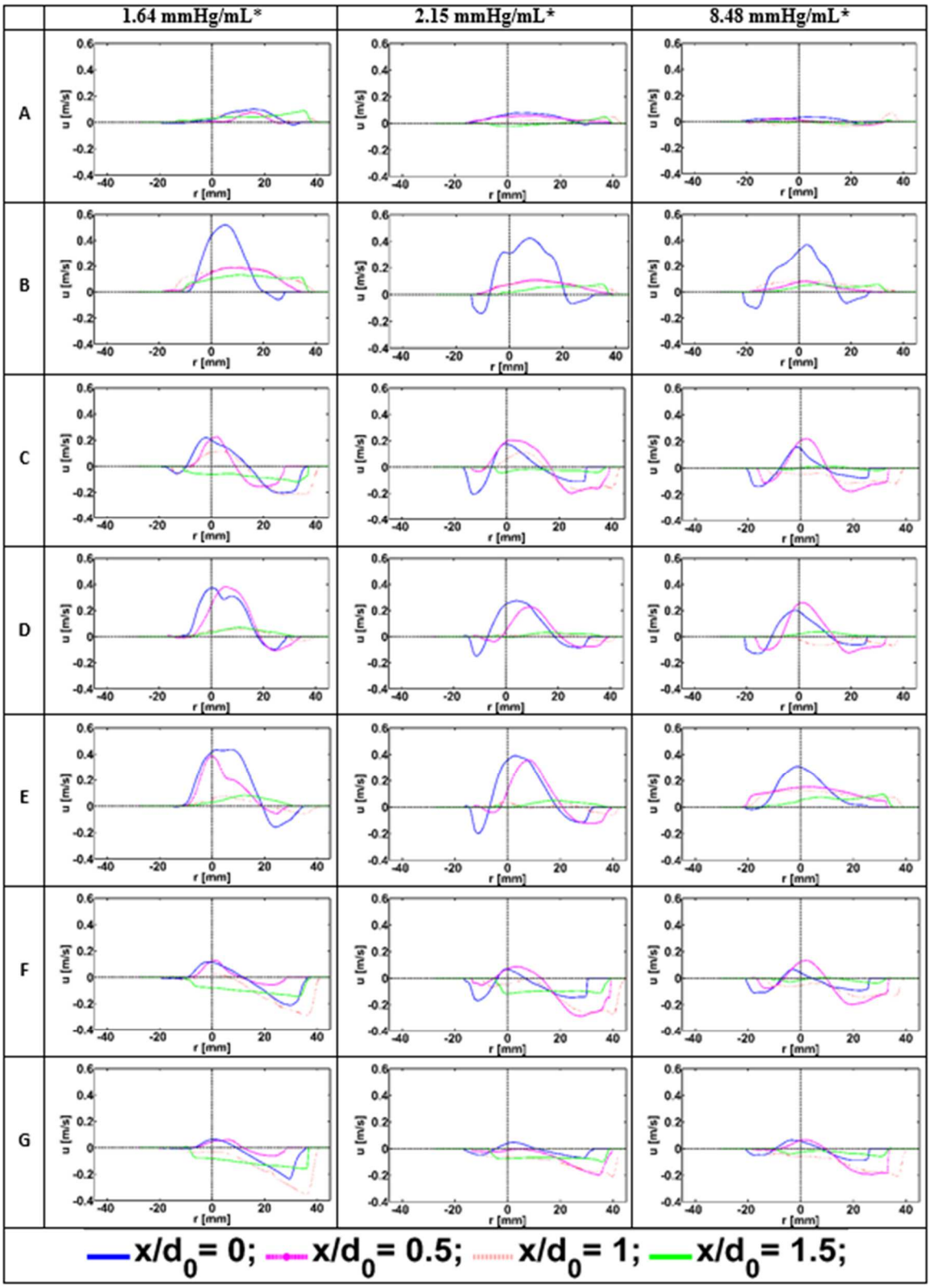

Table 15: 2D velocity profile downstream of the mitral valve at x/d_0 = 0, 0.5, 1, and 1.5 during the presence of A-wave; A)Zero flow, B)Acceleration phase, C) Peak E-wave, D) Diastasis, E) peak A-wave, F) Deceleration phase, and G) Peak closing volume

6.4 Circulation

After identifying the vortex ring using swirling strength criterion λ_{ci} (described above), circulation strength (Γ) of the anterior (counter-clockwise rotating) vortex ring was calculated by integrating z-axis vorticity 'ω_z' over the rectangular region inside the LV as shown in the figure below.

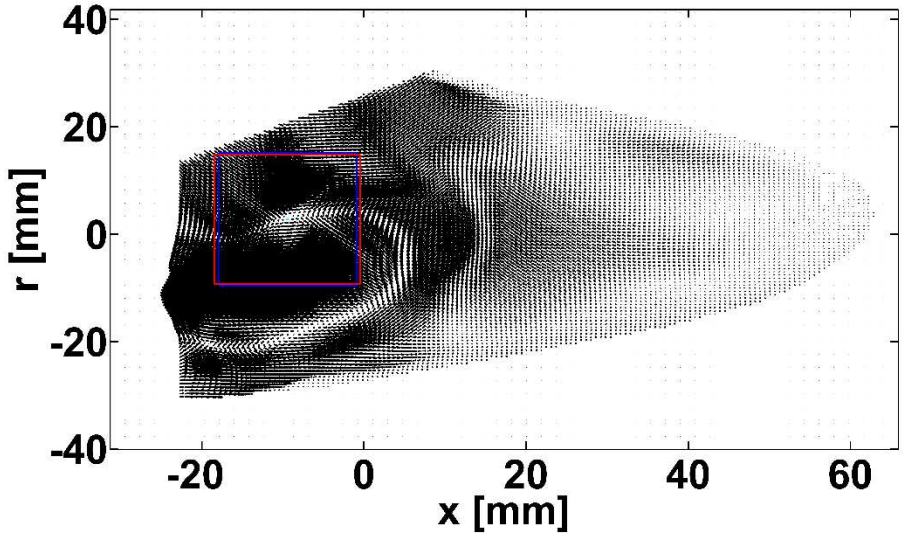

Figure 45: Circulation calculated over the rectangular region

The circulation strength (Γ) calculated at different phases of the diastole were plotted as a function of varying LV wall stiffness (mmHg/mL). Each individual curve shown in **Figure 46** and **Figure 47** corresponds to a unique LV wall stiffness (mmHg/mL) which are represented in a legend. Comparison of circulation strength among 3 LV physical model shows the strong effects of LV wall stiffness on the intensity and slope of circulation strength (Γ).

A) Circulation strength (absence of A-wave)

Figure 46 shows the variation in circulation strength (Γ) inside the LV during diastole with the absence of A-wave. The circulation values of least stiff model (1.64 mmHg/mL) in this plot starts at zero due to the absence of LV vortex ring which increases as the inflow jet reaches its peak inlet velocity. In the same model, the highest value of circulation (19.9 $\frac{m^2}{s}$) is attained

during the deceleration phase. Meanwhile, the most stiff models show reduced circulation strength (4.9 $\frac{m^2}{s}$ → 4.5 $\frac{m^2}{s}$) compared to the least stiff model.

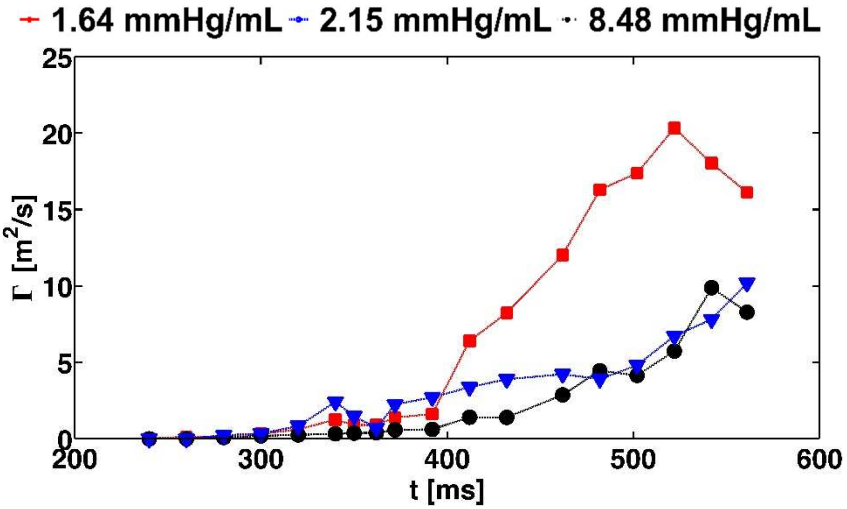

Figure 46: Circulation strength (Γ) plotted as a function of varying LV wall stiffness over diastolic phase of the cardiac cycle during the absence of A-wave

B) Circulation strength (presence of A-wave)

Figure 47 shows the variation in circulation strength (Γ) inside the LV during diastole with the presence of A-wave. The circulation in this plot follows the same trend wherein the values start at 4.3 $\left(\frac{m}{s}\right)^2$ and increase exponentially as the inflow jet reaches its peak inlet velocity. In the least stiff (1.64 mmHg/mL) model, the 1st highest value of circulation (15.5 $\left(\frac{m}{s}\right)^2$) is attained during the Peak-E wave. Meanwhile, the most stiff models show reduced circulation strength (8.8 $\left(\frac{m}{s}\right)^2$ → 6.0 $\left(\frac{m}{s}\right)^2$) compared to the least stiff model. The 2nd highest circulation value is seen during the A-wave in the least stiff model (14.5 $\left(\frac{m}{s}\right)^2$), while the other two models show reduced circulation strength (10.5 $\left(\frac{m}{s}\right)^2$ → 8.9 $\left(\frac{m}{s}\right)^2$).

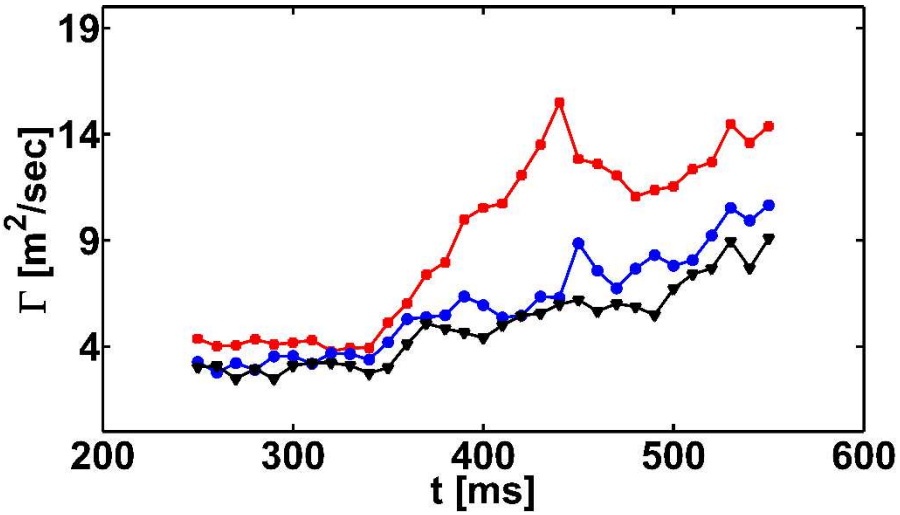

Figure 47: Circulation strength (Γ) plotted as a function of varying LV wall stiffness over diastolic phase of the cardiac cycle during the presence of A-wave

6.5 Energetics

Energy exists in different forms inside the heart in terms of pressure, electrical impulse, kinetic energy etc. In this section, we will take a close look at kinetic energy and its dissipation rate throughout diastolic phase of the cardiac cycle. Each individual curve shown in **Figure 48** and **Figure 49** corresponds to a unique LV wall stiffness (mmHg/mL) which are represented in a legend.

6.5.1 Kinetic energy

According to the law of conservation of mass, the increase in velocity magnitude of the inflow jet during diastole, causes a spike in kinetic energy inside the LV. This kinetic energy is stored inside the vortex rings formed during diastole and released during systole. Therefore, kinetic energy plays a huge role in LV filling and pumping fluid dynamics. The total kinetic energy ($E_k \left(\frac{m}{s}\right)^2$) calculated inside the LV field of view was plotted as a function of varying LV wall stiffness with respect to the dimensionless time (t*) across the diastolic phase of the cardiac cycle.

A) Kinetic energy (absence of A-wave)

Figure 48Figure 48: Kinetic energy plotted as a function of varying LV wall stiffness and dimensionless time with the absence of A-wave shows kinetic energy plotted as a function of varying LV wall stiffness with the absence of A-wave. The kinetic energy inside the LV increases as the flow starts coming in during diastole and drops considerably during systole. This plot shows kinetic energy in the least stiff model (1.64 mmHg/mL) reaching its highest value (178 $\left(\frac{m}{s}\right)^2$), which reduced in the other two models (131 $\left(\frac{m}{s}\right)^2$, 110 $\left(\frac{m}{s}\right)^2$).

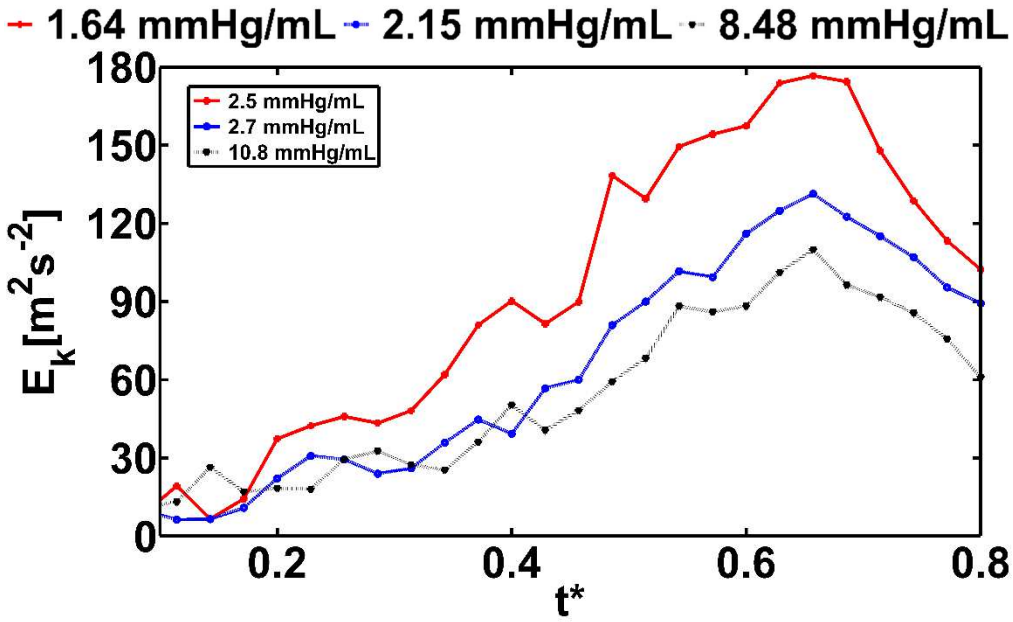

Figure 48: Kinetic energy plotted as a function of varying LV wall stiffness and dimensionless time with the absence of A-wave

B) Kinetic energy (presence of A-wave)

Figure 49 shows kinetic energy plotted as a function of varying LV wall stiffness with the presence of A-wave. Similar trend is seen in the plot, where the kinetic energy inside the LV increases as the flow starts coming in during diastole and drops considerably during systole. This plot shows kinetic energy in the least stiff model (1.64 mmHg/mL) reaching its highest values at the peak E-wave (76.8 $\left(\frac{m}{s}\right)^2$) and peak A-wave (74.8 $\left(\frac{m}{s}\right)^2$), which in the other two models were

seen to be reduced (56.6 $\left(\frac{m}{s}\right)^2$, 54.4 $\left(\frac{m}{s}\right)^2$) (2.15 mmHg/mL), (42.4 $\left(\frac{m}{s}\right)^2$, 42.5 $\left(\frac{m}{s}\right)^2$) (8.48 mmHg/mL).

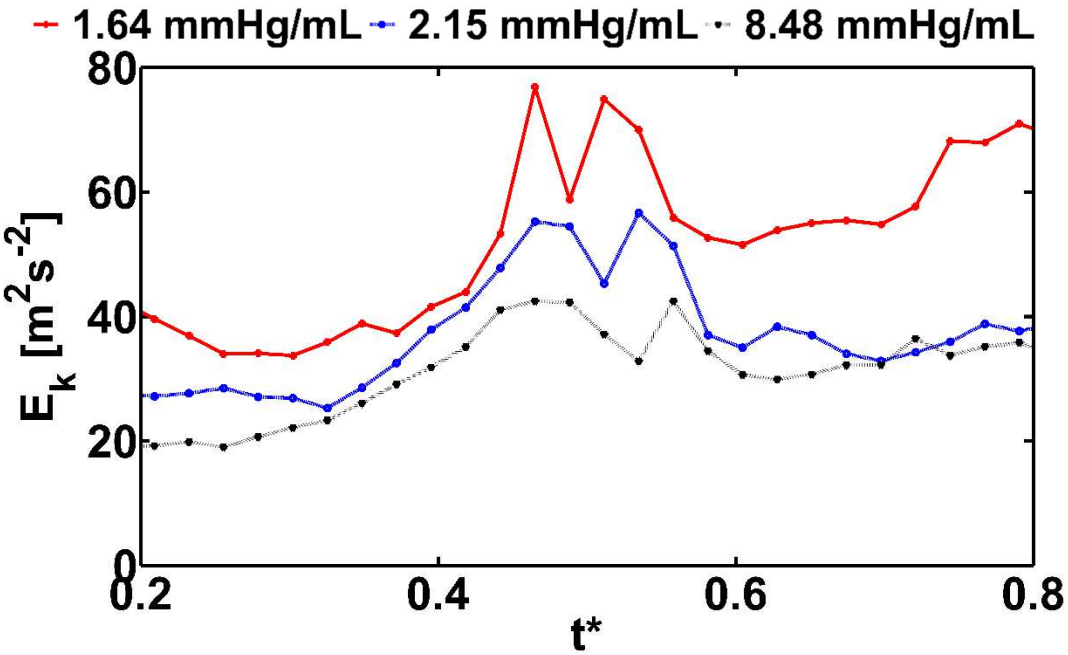

Figure 49: Kinetic energy plotted as a function of varying LV wall stiffness and dimensionless time with the presence of A-wave

6.5.2 Energy dissipation rate

Energy dissipation inside the LV dictates the amount of energy being lost by the fluid during a single cardiac cycle. Hence, energy dissipation has a direct impact on the LV hemodynamics which can cause reduction in LV efficiency. Energy dissipation rate ($\emptyset$ $\left(\frac{m^2}{s^3}\right)$) calculated inside the LV field of view was plotted as a function of varying LV wall stiffness with respect to the dimensionless time (t*) across the diastolic phase of the cardiac cycle.

A) Energy dissipation rate (absence of A-wave)

Figure 50 shows energy dissipation rate inside the LV as a function of varying LV wall stiffness with the absence of A-wave. The graph shows a decreasing trend among LV physical models, where the peak energy dissipation rate dropped from (64.8 $\left(\frac{m^2}{s^3}\right)$) in the least stiff model to (51.6 $\left(\frac{m^2}{s^3}\right)$,38.5 $\left(\frac{m^2}{s^3}\right)$) in the other two models.

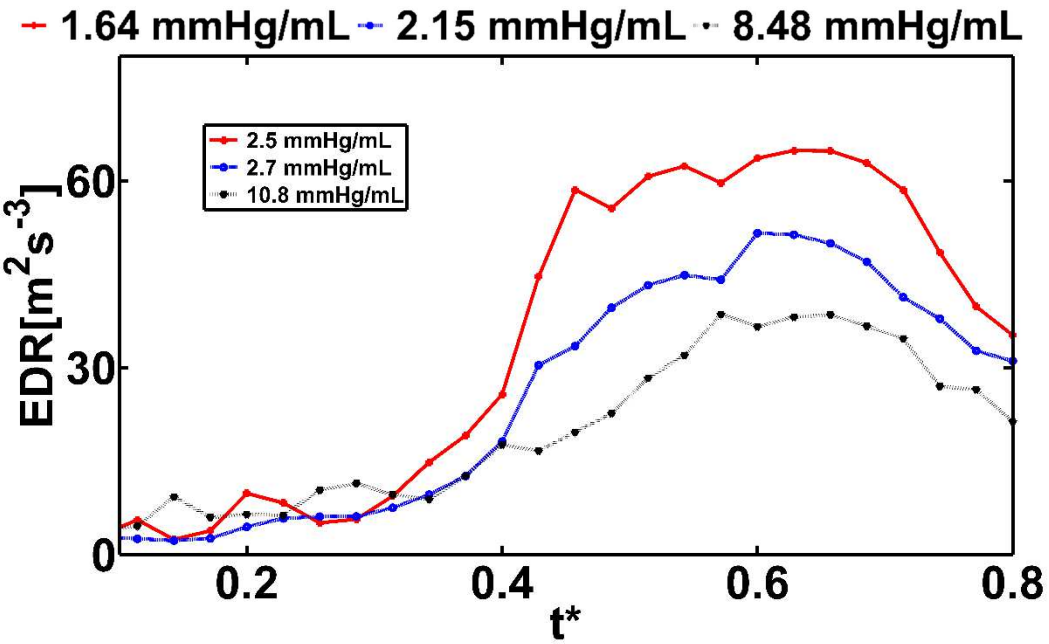

Figure 50: Energy dissipation rate plotted as a function of varying LV wall stiffness and dimensionless time with the absence of A-wave

B) Energy dissipation rate (presence of A-wave)

Figure 51 shows energy dissipation rate (EDR) inside the LV as a function of varying LV wall stiffness with the presence of A-wave. In addition to the decreasing trend seen among LV physical models, the graph also shows two peaks each at peak E-wave and peak A-wave. The EDR at peak E-wave dropped from (55.7 $\left(\frac{m^2}{s^3}\right)$) in the least stiff model to (44.0 $\left(\frac{m^2}{s^3}\right)$, 38.0 $\left(\frac{m^2}{s^3}\right)$) in the other two models. And, EDR at peak A-wave dropped from (52.8 $\left(\frac{m^2}{s^3}\right)$) in the least stiff model to (39.4 $\left(\frac{m^2}{s^3}\right)$, 28.6 $\left(\frac{m^2}{s^3}\right)$) in the other two models.

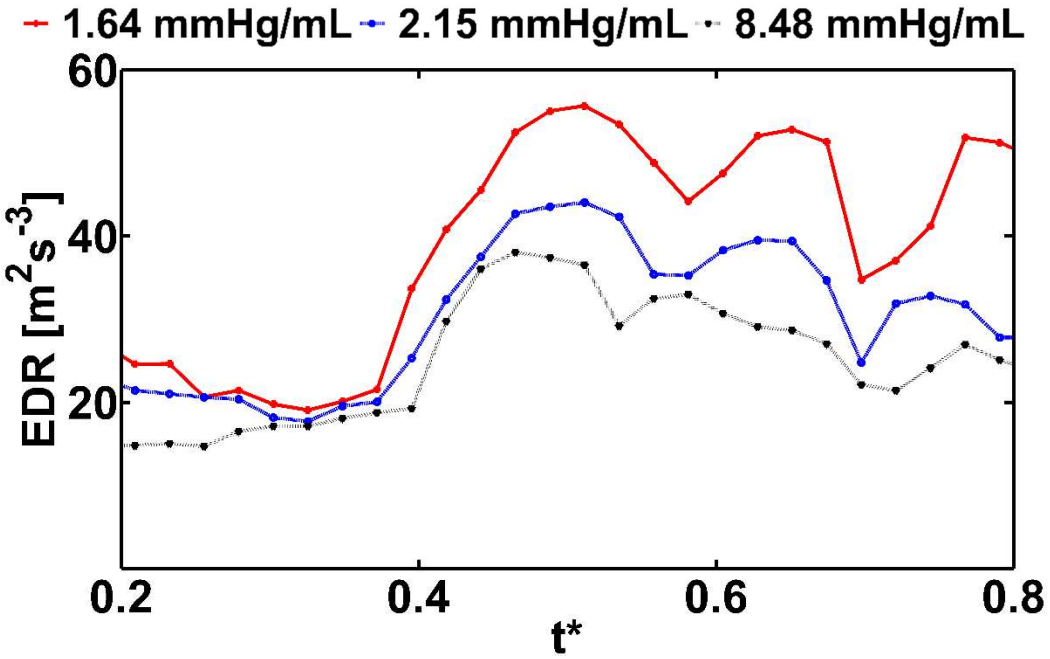

Figure 51: Energy dissipation rate plotted as a function of varying LV wall stiffness and dimensionless time with the presence of A-wave

CHAPTER VII

DISCUSSION

Half of the patients diagnosed with heart failure exhibit preserved ejection fraction (HFpEF) which has morbidity and mortality similar to that of patients exhibiting symptoms of heart failure with reduced ejection fraction (HFrEF). This makes diagnosis of HFpEF very challenging, often requiring invasive clinical assessments using monitoring techniques like pulse oximetry, pulmonary artery catheter etc. Previous studies of non-invasive imaging helped us understand the characteristics of intraventricular fluid dynamics, especially, vortex ring development inside the LV of a healthy individual [16]. On the other hand, simultaneous studies of steady streaming analysis in a patient diagnosed with diastolic cardiomyopathy (DCM) revealed alterations in LV vortex ring inside a geometrically altered LV [18]. This brings us to the underlying research question, does myocardial (LV wall) stiffening with preserved LV shape effect intraventricular fluid dynamics? And how can these changes be interpreted in order to help us diagnose a disease in its early stages. We hypothesized that, increase in myocardial (LV wall) stiffness with preserved LV profile will impair filling via diminished inflow circulation. In order to verify the hypothesis, we used an invitro LV model to compare baseline 'normal' LV model hemodynamics with varying stiffness models, while holding other circuit variables constant.

As a result of this study, we found that with the increase in LV wall stiffness, hemodynamic properties like aortic pressure, cardiac output, stroke volume, ejection fraction, E-wave duration, diastolic duration, and deceleration time decreased drastically, while, the E/A ratio and A-wave duration increased exponentially. From a clinical perspective, these results show reduction in the LV performance while preserving the EF which can help us diagnose HFpEF prior to its permanent maladaptive alterations.

7.1 Clinical need for the study

Heart failure was considered to be caused due to reduced left ventricle performance, triggered by insufficient ejection fraction (<50%), until, research showed otherwise. Recent studies have helped us understand that heart failure can occur even when ejection fraction is preserved (>50%), also known as HFpEF [90-93]. According to national entries, out of all the heart failure patients diagnosed, 46 – 51% come under the category of HFpEF [94-96]. This indicates an unprecedented need to understand the characteristics of HFpEF in order to diagnose the condition in its early phase.

The two main criteria recommended for the diagnosis of HFpEF, as per the European society of cardiology (ESC) are echocardiography (cardiovascular imaging) and hemodynamic parameters (invasive measurement). According to ESC, general signs of HFpEF include presence of EF >50%, decrease in LV end-diastolic volume and existence of diastolic dysfunction [97]. Although cardiovascular imaging can be used to diagnose HFpEF, invasive measurements of hemodynamic parameters remain as a standard method of diagnosing this particular disease. In this study we used an invitro model with LV physical models of increasing wall stiffness in order to recreate HFpEF and observe its effects on hemodynamic parameters. Both cardiovascular images (PIV) and invasive measurements were obtained during our study which were analyzed and presented in the earlier chapter. Usage of these dual diagnostic techniques helped bridging the gap between them, which enabled us to detect HFpEF even during the absence of other.

7.2 Fluid dynamic observations

Although there is a strong relationship between LV vortex and LV performance, there is a lack of quantitative and qualitative information on LV vortex parameters like vorticity, LV vortex shape and size, kinetic energy etc. Previous studies have shown an increase in vortex area and intensity in computational models of LV with lower than average myocardial stiffness (DCM) [4, 36, 98]. Findings of this study are in harmony with the conclusions made in the literature, where we observed a decrease in size and intensity of the LV anterior vortex ring with the increase in LV wall stiffness. Conversely, a decrease in total kinetic energy was also observed with the increase in LV wall stiffness, due to a direct relationship between LV vortex and kinetic energy [99]. Additionally, flow stagnation which is known to facilitate thrombus formation among patients diagnosed with myocardial diseases [100] was observed inside the LV. Flow stagnation occurs due to the incapability of vortex penetration into the LV which in turn caused reduction in aortic (33%) and LV pressures (30%) during stiffness alterations.

The current study also revealed a significant decrease (43%) in inlet jet velocity magnitude, which is in coherence with the observations found in a study conducted on velocity propagation in early diastole using Colour M-mode [101]. Since, inlet jet velocity has a direct influence on peak E-wave [98], reduction in peak E-wave (22%) with the increase in LV wall stiffness was observed. Peak aortic flow, CO, SV, and EDV which are dependent on the E-wave, inlet velocity and LV vortex dropped 21%, 41%, 27% and 12% respectively as well. Meanwhile, EF dropped 7% but stayed above 50% preserving EF during the entire experiment. Presence of A-wave did not alter the hemodynamic trend, where atrial pressure, LVP, peak E-wave, CO, SV, diastolic duration, deceleration time, and EDV decreased 27%, 29%, 11%, 25%, 26%, 11%, 27%, 8% respectively. The E/A ratio however increased from 1.2 → 2.2 with the increase in LV wall stiffness, indicating a pattern of restrictive filling which is associated with increased LV stiffness [102].

7.3 Clinical significance of the findings

Many factors are listed as a cause of diastolic dysfunction (DD) and diastolic heart failure, the most important one being left ventricular stiffening. While, both cardiovascular imaging and invasive measurement are used together to diagnose diseases like HF. This study precisely focuses on non-invasive imaging technique (particle image velocimetry) to determine the hemodynamic changes during ventricular (myocardial) stiffening which can be used to detect early disease in patients at risk. Findings from this study demonstrate the potential for using the filling vortex circulation as a surrogate measure of LV wall stiffness in HFpEF patients. The LV vortex circulation can be determined using non-invasive 3D medical imaging techniques (phase-contrast magnetic resonance imaging, echocardiography) across multiple HFpEF patients, and compared to the values of LV stiffness using diastolic pressure-volume curves on the same patient population. Obtaining the latter typically relies on using pressure recordings using catheters and mitral Doppler inflow. The usage of circulation as a surrogate index of stiffness can thus simplify the process of diagnosis of HFpEF and remove the use of invasive catheterization.

7.4 Limitations

Although this study successfully satisfied its objectives, there were few inevitable limitations associated with it. Firstly, an in vitro model was used in the study instead of a biological model due to its simplicity, specificity and transferability. These models are mainly used in studies related to cells, tissues or biological molecules where the components are isolated or mechanically recreated/altered which permits a more detailed and convenient study. Secondly, the exact stiffness values for the LV physical models used in the study are not physiologically seen, but the relative changes between the models are still expected to be valid. Thirdly, the mechanical heart valves used in the study do not operate like the biological valves, but exhibit similar flow characteristics. Although these valves are prone to hemorrhage, thrombosis and other infections, due to the usage of blood mimicking fluid in this study makes these issues irrelevant. Finally, blood mimicking fluid (BMF) (glycerin-water mixture) was used in the study instead of

actual blood because of number of difficulties associated with it like shelf life, fluid properties, acoustical properties etc. BMF has been approved and used in many previous vitro studies consisting of imaging techniques like Doppler imaging, particle image velocimetry etc.

CHAPTER VIII

CONCLUSION

2D phase locked planar measurements inside the LV physical models using particle image velocimetry was performed in order to investigate the effects of LV wall stiffness on the hemodynamics and the flow structures. Time averaged flow properties, velocity fields, vorticity fields, velocity profiles and energetics have been displayed in the chapters above providing rich content of information. Increase in myocardial (LV wall) stiffness with preserved LV profile caused impaired filling via diminished inflow circulation.

The following variations were observed when the LV physical model stiffness was increased from least stiff to most stiff

- Overall decrease in the size and intensity of the LV vortex, aortic and LV pressures, kinetic energy, and dissipation rate were observed both with and without the presence of A-wave.
- During the absence of A-wave, the inlet jet velocity, peak E-wave, peak aortic flow, CO, SV, EDV, and EF dropped 43%, 22%, 21%, 41%, 27%, 12%, 7% respectively.
- During the presence of A-wave, the inlet jet velocity, peak E-wave, peak aortic flow, CO, SV, EDV, and EF dropped 22%, 11%, 29%, 25%, 26%, 8%, 13% respectively.
- E/A ratio increased from 1.2 → 2.2 during the presence of A-wave.

8.1 Recommendations for future work

Although the results obtained during this study answered the research question, it could be further extended and developed in multiple ways.

8.1.1 Incorporating exercise conditions

The hemodynamics and flow characteristics observed in the heart during exercise conditions (100+ BPM) are slightly different when compared to the resting condition (70 BPM). This study was mainly focused on resting conditions with and without the presence of A-wave. Repeating the experiments with multiple heart rates at exercise frequency may provide additional information that will shed some light on hemodynamics during stressful conditions.

8.1.2 Incorporating left ventricular rotation and twist

Previous studies have shown that physiologically, heart rotates along its long-axis with a twisting motion [103]. The LV physical model used in the current experiment does not exhibit rotation or twisting motions during the cardiac cycle due to the mechanical complexities. Perhaps, by incorporating these motions (individually or together) we could obtain more physiological and reliable LV flow characteristics. This could potentially change the observations seen during this study entirely which will be interesting to check.

8.1.3 Testing LV physical models with varying profiles

Heart failure can occur due to multiple factors like obstructive hypertrophic cardiomyopathy, ventricular hypertrophy, ventricular dilation etc. The dimensions of the LV physical model used in this experiment resembles a healthy human LV. Designing LV models for future experiments while incorporating dimensions measured from patients diagnosed with diseases like obstructive hypertrophic cardiomyopathy, hypertrophic cardiomyopathy, dilated cardiomyopathy etc. will show changes, if there are any in LV hemodynamics as a function of LV profile.

REFERENCES

1. Roger, V.L., et al., *Heart disease and stroke statistics--2012 update: a report from the American Heart Association.* Circulation, 2012. **125**(1): p. e2-e220.
2. Braunwald, E., et al., *Harrison's Principles of Internal Medicine*. McGraw-Hill.
3. Murphy, S.L., J. Xu, and K.D. Kochanek, *Deaths: final data for 2010.* Natl Vital Stat Rep, 2013. **61**(4): p. 1-117.
4. García, M.J., *Diagnosis and Therapeutic Guidance of Diastolic Heart Failure.* Revista Española de Cardiología (English Version), 2003. **56**(04): p. 396-406.
5. Kilner, P.J., et al., *Asymmetric redirection of flow through the heart.* Nature, 2000. **404**(6779): p. 759-761.
6. Kim, W.Y., et al., *Two-dimensional mitral flow velocity profiles in pig models using epicardial Doppler echocardiography.* J Am Coll Cardiol, 1994. **24**(2): p. 532-45.
7. Kim, W.Y., et al., *Left ventricular blood flow patterns in normal subjects: a quantitative analysis by three-dimensional magnetic resonance velocity mapping.* J Am Coll Cardiol, 1995. **26**(1): p. 224-38.
8. Borazjani, I., et al., *Left Ventricular Flow Analysis: Recent Advances in Numerical Methods and Applications in Cardiac Ultrasound.* Computational and Mathematical Methods in Medicine, 2013. **2013**: p. 395081.
9. Bellhouse, B.J., *Fluid mechanics of a model mitral valve and left ventricle.* Cardiovasc Res, 1972. **6**(2): p. 199-210.
10. Reul, H., N. Talukder, and E.W. Mu¨ller, *Fluid mechanics of the natural mitral valve.* Journal of Biomechanics, 1981. **14**(5): p. 361-372.
11. DIAMOND, G. and J.S. FORRESTER, *Effect of Coronary Artery Disease and Acute Myocardial Infarction on Left Ventricular Compliance in Man.* Circulation, 1972. **45**(1): p. 11-19.
12. Diamond, G., et al., *Diastolic pressure-volume relationship in the canine left ventricle.* Circ Res, 1971. **29**(3): p. 267-75.
13. Forrester, J.S., et al., *Filling Pressures in the Right and Left Sides of the Heart in Acute Myocardial Infarction.* New England Journal of Medicine, 1971. **285**(4): p. 190-193.

14. Forrester, J.S., et al., *Early Increase in Left Ventricular Compliance after Myocardial Infarction.* Journal of Clinical Investigation, 1972. **51**(3): p. 598-603.
15. Hood, W.B., Jr., et al., *Experimental myocardial infarction. IV. Reduction of left ventricular compliance in the healing phase.* J Clin Invest, 1970. **49**(7): p. 1316-23.
16. Pedrizzetti, G., et al., *The vortex[mdash]an early predictor of cardiovascular outcome?* Nat Rev Cardiol, 2014. **11**(9): p. 545-553.
17. Mangual, J.O., et al., *Comparative numerical study on left ventricular fluid dynamics after dilated cardiomyopathy.* Journal of Biomechanics, 2013. **46**(10): p. 1611-1617.
18. Kheradvar, A., et al., *Echocardiographic Particle Image Velocimetry: A Novel Technique for Quantification of Left Ventricular Blood Vorticity Pattern.* Journal of the American Society of Echocardiography, 2010. **23**(1): p. 86-94.
19. Chan, B.T., et al. *Simulation of left ventricle flow dynamics with dilated cardiomyopathy during the filling phase*. in *Engineering in Medicine and Biology Society (EMBC), 2012 Annual International Conference of the IEEE*. 2012.
20. Pasipoularides, A., *Fluid dynamics of ventricular filling in heart failure: overlooked problems of RV/LV chamber dilatation.* Hellenic J Cardiol, 2015. **56**(1): p. 85-95.
21. Mehregan, F., et al., *Doppler vortography: a color Doppler approach for quantification of the intraventricular blood flow vortices.* Ultrasound in medicine & biology, 2014. **40**(1): p. 10.1016/j.ultrasmedbio.2013.09.013.
22. Cimino, S., et al., *In vivo analysis of intraventricular fluid dynamics in healthy hearts.* European Journal of Mechanics - B/Fluids, 2012. **35**(0): p. 40-46.
23. Agati, L., et al., *Quantitative analysis of intraventricular blood flow dynamics by echocardiographic particle image velocimetry in patients with acute myocardial infarction at different stages of left ventricular dysfunction.* Eur Heart J Cardiovasc Imaging, 2014. **15**(11): p. 1203-12.
24. Betts, J.G., et al., *Anatomy and Physiology*. 2013.
25. Gray, H. and W.H. Lewis, *Anatomy of the human body*. 1918, Philadelphia: Lea & Febiger.
26. Ken Young Lin, E.R.E., Gary Strichartz, Leonard S. Lilly, *Pathophysiology of Heart Disease*. 5th ed, ed. L.S. Lilly. 2011, Baltimore, MD: Lippincott Williams & Wilkins. 437.
27. Starr, C., C. Evers, and L. Starr, *Biology Today and Tomorrow with Physiology*. 2009: Cengage Learning.
28. Ghosh, E., *Multi- Modal Characterization Of Left Ventricular Diastolic Filling Physiology*. 2014, Washington University: All Theses and Dissertations (ETDs). p. 237.
29. Dorland and W.A.N. Dorland, *Dorland's Illustrated Medical Dictionary32: Dorland's Illustrated Medical Dictionary*. 2011: Elsevier/Saunders.
30. Fukuta, H. and W.C. Little, *The Cardiac Cycle and the Physiological Basis of Left Ventricular Contraction, Ejection, Relaxation, and Filling.* Heart failure clinics, 2008. **4**(1): p. 1-11.

31. Lind, B., et al., *Left ventricular isovolumic velocity and duration variables calculated from colour-coded myocardial velocity images in normal individuals.* European Heart Journal - Cardiovascular Imaging, 2004. **5**(4): p. 284-293.
32. Price, D., *How to read an Electrocardiogram (ECG). Part One: Basic principles of the ECG. The normal ECG.* South Sudan Medical Journal, 2010. **3**(4): p. 26-28.
33. Antz, M., et al., *Electrical conduction between the right atrium and the left atrium via the musculature of the coronary sinus.* Circulation, 1998. **98**(17): p. 1790-5.
34. De Ponti, R., et al., *Electroanatomic Analysis of Sinus Impulse Propagation in Normal Human Atria.* Journal of Cardiovascular Electrophysiology, 2002. **13**(1): p. 1-10.
35. Szu, H., et al. *Smartphone home monitoring of ECG*. 2012.
36. Baccani, B., et al., *Fluid dynamics of the left ventricular filling in dilated cardiomyopathy.* J Biomech, 2002. **35**(5): p. 665-71.
37. Long, Q., et al., *The Influence of Inflow Boundary Conditions on Intra Left Ventricle Flow Predictions.* Journal of Biomechanical Engineering, 2004. **125**(6): p. 922-927.
38. Saber, N.R., et al., *Computational flow modeling of the left ventricle based on in vivo MRI data: initial experience.* Ann Biomed Eng, 2001. **29**(4): p. 275-83.
39. Hong, G.-R., et al., *Characterization and Quantification of Vortex Flow in the Human Left Ventricle by Contrast Echocardiography Using Vector Particle Image Velocimetry.* JACC: Cardiovascular Imaging, 2008. **1**(6): p. 705-717.
40. Peskin, C.S. and D.M. McQueen, *A three-dimensional computational method for blood flow in the heart I. Immersed elastic fibers in a viscous incompressible fluid.* Journal of Computational Physics, 1989. **81**(2): p. 372-405.
41. Kilner, P.J., et al., *Asymmetric redirection of flow through the heart.* Nature, 2000. **404**(6779): p. 759-61.
42. Gharib, M., et al., *Optimal vortex formation as an index of cardiac health.* Proc Natl Acad Sci U S A, 2006. **103**(16): p. 6305-8.
43. Pedrizzetti, G. and F. Domenichini, *Nature optimizes the swirling flow in the human left ventricle.* Phys Rev Lett, 2005. **95**(10): p. 108101.
44. Kim, D.-H., et al., *Determinants of Left Ventricular Vortex Flow Parameters Assessed by Contrast Echocardiography in an In Vivo Animal Model.* Echocardiography, 2013. **30**(5): p. 588-598.
45. Zhang, H., et al., *The Evolution of Intraventricular Vortex during Ejection Studied by Using Vector Flow Mapping.* Echocardiography, 2013. **30**(1): p. 27-36.
46. Hong, G.-R., et al., *Current Clinical Application of Intracardiac Flow Analysis Using Echocardiography.* J Cardiovasc Ultrasound, 2013. **21**(4): p. 155-162.
47. Schlosser, T., et al., *Assessment of Left Ventricular Parameters Using 16-MDCT and New Software for Endocardial and Epicardial Border Delineation.* American Journal of Roentgenology, 2005. **184**(3): p. 765-773.
48. Guyton, A.C. and J.E. Hall, *Textbook of Medical Physiology*. 2006: Elsevier Saunders.
49. Jefferies, J.L. and J.A. Towbin, *Dilated cardiomyopathy.* Lancet, 2010. **375**(9716): p. 752-62.

50. Courtois, M., S.J. Kovacs, Jr., and P.A. Ludbrook, *Transmitral pressure-flow velocity relation. Importance of regional pressure gradients in the left ventricle during diastole.* Circulation, 1988. **78**(3): p. 661-71.
51. Appleton, C.P., L.K. Hatle, and R.L. Popp, *Relation of transmitral flow velocity patterns to left ventricular diastolic function: new insights from a combined hemodynamic and Doppler echocardiographic study.* J Am Coll Cardiol, 1988. **12**(2): p. 426-40.
52. Grossman, W., L.P. McLaurin, and E.L. Rolett, *Alterations in left ventricular relaxation and diastolic compliance in congestive cardiomyopathy.* Cardiovasc Res, 1979. **13**(9): p. 514-22.
53. Ishida, Y., et al., *Left ventricular filling dynamics: influence of left ventricular relaxation and left atrial pressure.* Circulation, 1986. **74**(1): p. 187-96.
54. Vanoverschelde, J.-L.J., et al., *Left ventricular filling in dilated cardiomyopathy: Relation to functional class and memodynamics.* Journal of the American College of Cardiology, 1990. **15**(6): p. 1288-1295.
55. Maron, B.J., et al., *American College of Cardiology/European Society of Cardiology Clinical Expert Consensus Document on Hypertrophic Cardiomyopathy: a report of the American College of Cardiology Foundation Task Force on Clinical Expert Consensus Documents and the European Society of Cardiology Committee for Practice Guidelines.* Journal of the American College of Cardiology, 2003. **42**(9): p. 1687-1713.
56. Mandinov, L., et al., *Diastolic heart failure.* Cardiovascular Research, 2000. **45**(4): p. 813-825.
57. Spirito, P. and B.J. Maron, *Significance of left ventricular outflow tract cross-sectional area in hypertrophic cardiomyopathy: a two-dimensional echocardiographic assessment.* Circulation, 1983. **67**(5): p. 1100-8.
58. Henry, W.L., et al., *Mechanism of left ventricular outlfow obstruction in patients with obstructive asymmetric septal hypertrophy (idiopathic hypertrophic subaortic stenosis).* Am J Cardiol, 1975. **35**(3): p. 337-45.
59. Wigle, E.D., *Hypertrophic cardiomyopathy: a 1987 viewpoint.* Circulation, 1987. **75**(2): p. 311-22.
60. Borlaug, B.A. and W.J. Paulus, *Heart failure with preserved ejection fraction: pathophysiology, diagnosis, and treatment.* European Heart Journal, 2011. **32**(6): p. 670-679.
61. Bursi, F., et al., *SYstolic and diastolic heart failure in the community.* JAMA, 2006. **296**(18): p. 2209-2216.
62. Talley, N.J. and S. O'Connor, *Examination medicine : [a guide to physician training]*. 2010, Sydney; New York: Churchill Livingstone Elsevier.
63. Little, W.C. and C.P. Cheng, *Left ventricular-arterial coupling in conscious dogs.* Am J Physiol, 1991. **261**(1 Pt 2): p. H70-6.
64. Little, W.C. and M. Pu, *Left ventricular-arterial coupling.* J Am Soc Echocardiogr, 2009. **22**(11): p. 1246-8.
65. Poh, K.K., et al., *Left ventricular fluid dynamics in heart failure: echocardiographic measurement and utilities of vortex formation time.* European Heart Journal - Cardiovascular Imaging, 2012. **13**(5): p. 385-393.

66. Hanrath, P., et al., *Left ventricular relaxation and filling pattern in different forms of left ventricular hypertrophy: An echocardiographic study.* The American Journal of Cardiology, 1980. **45**(1): p. 15-23.
67. Sanderson, J.E., et al., *Left ventricular filling in hypertrophic cardiomyopathy. An angiographic study.* British Heart Journal, 1977. **39**(6): p. 661-670.
68. Soufer, R., et al., *Intact systolic left ventricular function in clinical congestive heart failure.* The American Journal of Cardiology, 1985. **55**(8): p. 1032-1036.
69. Borlaug, B.A., et al., *Exercise hemodynamics enhance diagnosis of early heart failure with preserved ejection fraction.* Circ Heart Fail, 2010. **3**(5): p. 588-95.
70. Westermann, D., et al., *Role of left ventricular stiffness in heart failure with normal ejection fraction.* Circulation, 2008. **117**(16): p. 2051-60.
71. Adrian, R.J., K.T. Christensen, and Z.C. Liu, *Analysis and interpretation of instantaneous turbulent velocity fields.* Experiments in Fluids, 2000. **29**(3): p. 275-290.
72. Okafor, I., et al., *Cardiovascular magnetic resonance compatible physical model of the left ventricle for multi-modality characterization of wall motion and hemodynamics.* Journal of Cardiovascular Magnetic Resonance, 2015. **17**(1): p. 51.
73. Frank, O., *The basic shape of the arterial pulse. First treatise: Mathematical analysis.* Journal of Molecular and Cellular Cardiology, 1990. **22**(3): p. 255-277.
74. Sagawa, K., R.K. Lie, and J. Schaefer, *Translation of Otto frank's paper "Die Grundform des arteriellen Pulses" zeitschrift für biologie 37: 483–526 (1899).* Journal of Molecular and Cellular Cardiology, 1990. **22**(3): p. 253-254.
75. Trevan, J.W., *The Viscosity of Blood.* Biochemical Journal, 1918. **12**(1-2): p. 60-71.
76. Dasi, L.P., et al., *FLUID MECHANICS OF ARTIFICIAL HEART VALVES.* Clinical and experimental pharmacology & physiology, 2009. **36**(2): p. 225-237.
77. Travis, B.R., et al., *Bileaflet aortic valve prosthesis pivot geometry influences platelet secretion and anionic phospholipid exposure.* Ann Biomed Eng, 2001. **29**(8): p. 657-64.
78. Feng, Z., et al., *In vitro investigation of opening behavior and hydrodynamics of bileaflet valves in the mitral position.* Artif Organs, 2002. **26**(1): p. 32-9.
79. Govindarajan, V., et al., *Impact of Design Parameters on Bi-leaflet Mechanical Heart Valve Flow Dynamics.* The Journal of heart valve disease, 2009. **18**(5): p. 535-545.
80. Quaini, A., et al., *A Three-Dimensional Computational Fluid Dynamics Model of Regurgitant Mitral Valve Flow: Validation Against in vitro Standards and 3D Color Doppler Methods.* Cardiovascular engineering and technology, 2011. **2**(2): p. 77-89.
81. Lee, D.-H., et al., *The Measurement of Opening Angle and Orifice Area of a Bileaflet Mechanical Valve Using Multidetector Computed Tomography.* Korean Circulation Journal, 2009. **39**(4): p. 157-162.
82. Lee, H., E. Tatsumi, and Y. Taenaka, *Experimental Study on the Reynolds and Viscous Shear Stress of Bileaflet Mechanical Heart Valves in a Pneumatic Ventricular Assist Device.* ASAIO Journal, 2009. **55**(4): p. 348-354.

83. Kurian, V.M.C., IN), *IMPLANTABLE MECHANICAL HEART VALVE ASSEMBLY*. 2010: United States.
84. Levine, P.A., *Industry Viewpoint: St. Jude Medical: Pacemakers, ICDs and MRI.* Pacing and Clinical Electrophysiology, 2005. **28**(4): p. 266-267.
85. *Theory of cross-correlation analysis of PIV images.* Applied Scientific Research, 1992. **49**(3): p. 191.
86. *Particle image velocimetry: improving fringe quality with a negative-mask method.* Applied Optics, 1995. **34**(11): p. 1763.
87. Andrea, S., et al., *Collaborative framework for PIV uncertainty quantification: comparative assessment of methods.* Measurement Science and Technology, 2015. **26**(7): p. 074004.
88. Okafor IU, S.A., Chaffins BD, Mirabella L, Oshinski JN, Yoganathan AP, *Cardiovascular magnetic resonance compatible physical model of the left ventricle for multi-modality characterization of wall motion and hemodynamics.* J Cardiovasc Magn Reson, to appear., 2015.
89. ZHOU, J.a.A., R. J. and BALACHANDAR,S. and KENDALL,T. M., *Mechanisms for generating coherent packets of hairpin vortices in channel flow.* Journal of Fluid Mechanics, 1999. **387**: p. 353-396.
90. *The survival of patients with heart failure with preserved or reduced left ventricular ejection fraction: an individual patient data meta-analysis.* European Heart Journal, 2012. **33**(14): p. 1750-1757.
91. Guazzi, M., *Pulmonary Hypertension in Heart Failure Preserved Ejection Fraction: Prevalence, Pathophysiology, and Clinical Perspectives.* Circulation: Heart Failure, 2014. **7**(2): p. 367-377.
92. Maeder, M.T. and D.M. Kaye, *Heart Failure With Normal Left Ventricular Ejection Fraction.* Journal of the American College of Cardiology, 2009. **53**(11): p. 905-918.
93. Sharma, K. and D.A. Kass, *Heart Failure With Preserved Ejection Fraction: Mechanisms, Clinical Features, and Therapies.* Circulation Research, 2014. **115**(1): p. 79-96.
94. Fonarow, G.C., et al., *Characteristics, Treatments, and Outcomes of Patients With Preserved Systolic Function Hospitalized for Heart Failure: A Report From the OPTIMIZE-HF Registry.* Journal of the American College of Cardiology, 2007. **50**(8): p. 768-777.
95. Lenzen, M.J., et al., *Differences between patients with a preserved and a depressed left ventricular function: a report from the EuroHeart Failure Survey.* European Heart Journal, 2004. **25**(14): p. 1214-1220.
96. Yancy, C.W., et al., *Clinical Presentation, Management, and In-Hospital Outcomes of Patients Admitted With Acute Decompensated Heart Failure With Preserved Systolic Function: A Report From the Acute Decompensated Heart Failure National Registry (ADHERE) Database.* Journal of the American College of Cardiology, 2006. **47**(1): p. 76-84.
97. Paulus, W.J., et al., *How to diagnose diastolic heart failure: a consensus statement on the diagnosis of heart failure with normal left ventricular ejection fraction by the Heart Failure and Echocardiography Associations of the*

European Society of Cardiology. European Heart Journal, 2007. **28**(20): p. 2539-2550.
98. Chan, B.T., et al., *Sensitivity Analysis of Left Ventricle with Dilated Cardiomyopathy in Fluid Structure Simulation.* PLoS ONE, 2013. **8**(6): p. e67097.
99. Bermejo, J., et al., *Intraventricular vortex properties in nonischemic dilated cardiomyopathy.* American Journal of Physiology - Heart and Circulatory Physiology, 2014. **306**(5): p. H718-H729.
100. Falk, R.H., E. Foster, and M.H. Coats, *Ventricular thrombi and thromboembolism in dilated cardiomyopathy: a prospective follow-up study.* Am Heart J, 1992. **123**(1): p. 136-42.
101. De Boeck, B.W., et al., *Colour M-mode velocity propagation: a glance at intra-ventricular pressure gradients and early diastolic ventricular performance.* Eur J Heart Fail, 2005. **7**(1): p. 19-28.
102. Masutani, S., et al., *Restrictive Left Ventricular Filling Pattern Does Not Result From Increased Left Atrial Pressure Alone.* Circulation, 2008. **117**(12): p. 1550-1554.
103. Nakatani, S., *Left Ventricular Rotation and Twist: Why Should We Learn?* Journal of Cardiovascular Ultrasound, 2011. **19**(1): p. 1-6.

APPENDICES

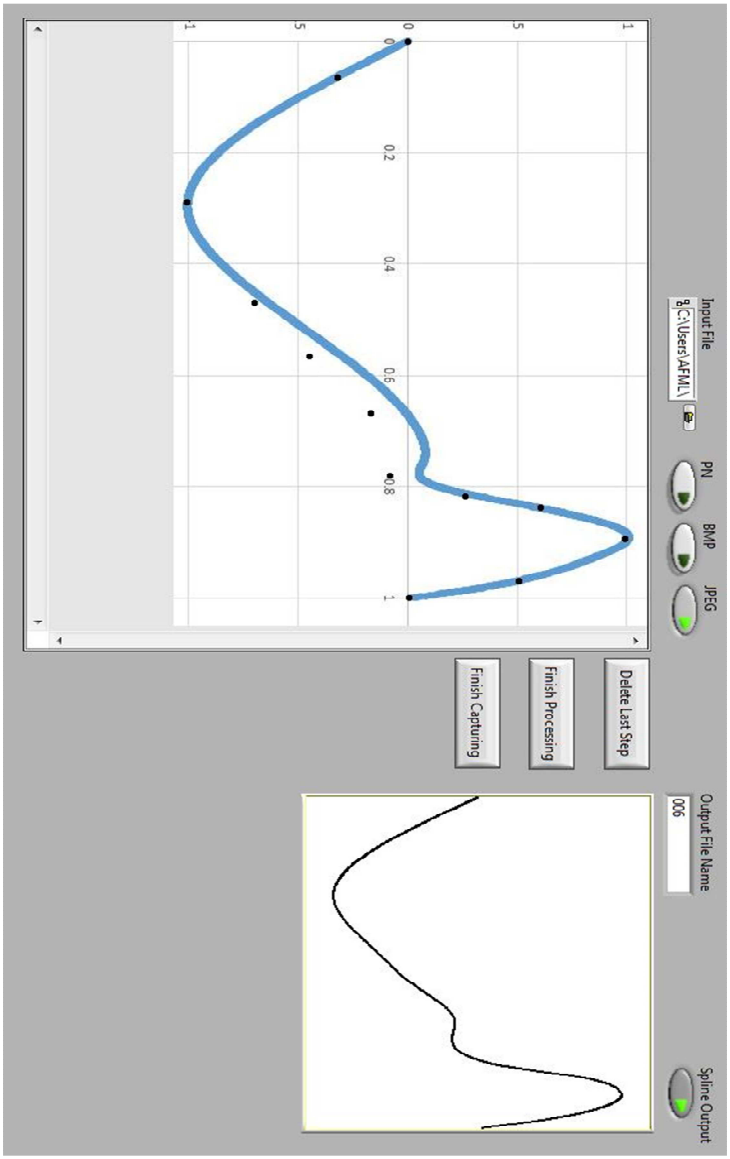

Figure 52: Screenshot of LabVIEW program used to generate custom waveforms for the SuperPump

VITA

Pritam Sai Mekala

Candidate for the Degree of

Master of Science

Thesis: COMPARATIVE STUDY OF DIASTOLIC FILLING UNDER VARYING LEFT VENTRICULAR WALL STIFFNESS

Major Field: Mechanical and Aerospace Engineering

Biographical:

Education:

Completed the requirements for the Master of Science in Mechanical and Aerospace Engineering at Oklahoma State University, Stillwater, Oklahoma in July, 2015.

Completed the requirements for the Bachelor of Science in Aeronautical Engineering at Vignan Institute of Technology and Aeronautical Engineering, Hyderabad, India in 2013.

Experience:

- Project leader at AFML (Stillwater, OK) Sep 2013 – present
- Designing biomedical components using SolidWorks/CAD for manufacturability (DFM).
- Experience in medical device design control, statistics and product development process.
- Maintaining detailed documentation of work instructions for builders and manufacturers.
- Writing validation and verification protocols on new/existing processes based on experimental results.
- Maintaining proper and complete documentation which meets quality requirements.
- Working hands-on with junior engineers, technicians, collaborators and test systems.

Professional Memberships:

IEEE, ASME/AIAA, APS-DFD.